

WALLABY Pilot Survey: the Potential Polar Ring Galaxies NGC 4632 and NGC 6156

N. Deg,^{1*} R. Palleske², K. Spekkens^{1,2}, J. Wang³, T. Jarrett⁴, J. English⁵, X. Lin³,
J. Yeung⁵, J. R. Mould⁶, B. Catinella^{7,8}, H. Dénes⁹, A. Elagali^{10,11}, B. -Q. For^{7,8},
P. Kamphuis¹², B.S. Koribalski^{13,14}, K. Lee-Waddell^{7,15,16}, C. Murugesan^{7,8}, S. Oh¹⁷,
J. Rhee^{7,8}, P. Serra¹⁸, T. Westmeier⁷, O.I. Wong^{15,7,8}, K. Bekki⁷, A. Bosma¹⁹,
C. Carignan^{4,20,21}, B.W. Holwerda²², N. Yu²³

¹Department of Physics, Engineering Physics, and Astronomy, Queen’s University, Kingston, ON, K7L 3N6, Canada

²Department of Physics and Space Science, Royal Military College of Canada, P.O. Box 17000, Station Forces Kingston ON K7K 7B4, Canada

³Kavli Institute for Astronomy and Astrophysics, Peking University, Beijing 100871, China

⁴Department of Astronomy, University of Cape Town, Private Bag X3, Rondebosch 7701, South Africa

⁵Department of Physics and Astronomy, University of Manitoba, Winnipeg, Manitoba, R3T 2N2, Canada

⁶Centre for Astrophysics & Supercomputing, Swinburne University, P.O.Box 218, Hawthorn, Vic 3122, Australia

⁷ICRAR - The University of Western Australia, 35 Stirling Highway, Crawley WA 6009, Australia

⁸ARC Centre of Excellence for All Sky Astrophysics in 3 Dimensions (ASTRO 3D), Australia

⁹School of Physical Sciences and Nanotechnology, Yachay Tech University, Hacienda San José S/N, 100119, Urcuquí, Ecuador

¹⁰Minderoo Foundation, 171 - 173 Mounts Bay Road, Perth, WA 6000, Australia

¹¹School of Biological Sciences, The University of Western Australia, 35 Stirling Highway, Crawley, WA 6009, Australia

¹²Ruhr University Bochum, Faculty of Physics and Astronomy, Astronomical Institute (AIRUB), 44780 Bochum, Germany

¹³CSIRO Space Science and Astronomy, Australia Telescope National Facility, P.O. Box 76, NSW 1710, Australia

¹⁴School of Science, Western Sydney University, Locked Bag 1797, Penrith, NSW 2751, Australia

¹⁵CSIRO Space and Astronomy, PO Box 1130, Bentley WA 6102, Australia

¹⁶ICRAR - Curtin University, Bentley, WA 6102, Australia

¹⁷Department of Physics and Astronomy, Sejong University, Seoul 05006, Korea

¹⁸INAF - Osservatorio Astronomico di Cagliari, Via della Scienza 5, I-09047 Selargius (CA), Italy

¹⁹Aix Marseille Univ, CNRS, CNES, LAM, Marseille

²⁰Département de physique, Université de Montréal, Complexe des sciences MIL, 1375 Avenue Thérèse-Lavoie-Roux Montréal, Qc, Canada H2V 0B3

²¹Laboratoire de Physique et de Chimie de l’Environnement, Observatoire d’Astrophysique de l’Université

Ouaga I Pr Joseph Ki-Zerbo (ODAUO), BP 7021, Ouaga 03, Burkina Faso

²²University of Louisville, Department of Physics and Astronomy, 102 Natural Science Building, 40292 KY Louisville, USA

²³National Astronomical Observatories, Chinese Academy of Sciences, 20A Datun Road, Chaoyang District, Beijing 100871, People’s Republic of China

Accepted XXX. Received YYY; in original form ZZZ

ABSTRACT

We report on the discovery of two potential polar ring galaxies (PRGs) in the WALLABY Pilot Data Release 1 (PDR1). These untargetted detections, cross-matched to NGC 4632 and NGC 6156, are some of the first galaxies where the HI observations show two distinct components. We used the IDAVIE virtual reality software to separate the anomalous gas from the galactic gas and find that the anomalous gas comprises $\sim 50\%$ of the total HI content of both systems. We have generated plausible 3D kinematic models for each galaxy assuming that the rings are circular and inclined at 90° to the galaxy bodies. These models show that the data are consistent with PRGs, but do not definitively prove that the galaxies are PRGs. By projecting these models at different combinations of main disk inclinations, ring orientations, and angular resolutions in mock datacubes, we have further investigated the detectability of similar PRGs in WALLABY. Assuming that these galaxies are indeed PRGs, the detectability fraction, combined with the size distribution of WALLABY PDR1 galaxies, implies an incidence rate of $\sim 1\% - 3\%$. If this rate holds true, the WALLABY survey will detect hundreds of new polar ring galaxies.

Key words: galaxies: peculiar – radio lines: galaxies

1 INTRODUCTION

Polar ring galaxies (PRGs) – systems which exhibit a ring or disk of material oriented perpendicular to the main disk – are some of the most visually striking objects in the Universe. An extreme among the variety of kinematically-misaligned structures detected in galaxies that includes warps and counter-rotating disks (Serra et al. 2014), PRGs hold important clues for galaxy structure and evolution that range from constraining how galaxies interact (e.g. Bekki 1997; Bournaud & Combes 2003; Reshetnikov & Sotnikova 1997) and accrete their gas (e.g. Macciò et al. 2006; Brook et al. 2008; Khoperskov et al. 2021), to probing the shapes and distributions of the dark matter halos in which they reside (e.g. Sackett & Sparke 1990; Combes & Arnaboldi 1996; Khoperskov et al. 2014).

Since the discovery of the first putative stellar polar structures around nearby galaxies (Sandage 1961; Schechter & Gunn 1978), there have been a number of attempts to measure their incidence in large optical surveys. Whitmore et al. (1990) searched for polar structures around S0 galaxies and generated a catalogue of 157 PRG candidates. They confirmed that PRGs require kinematic followups to determine that the polar material is indeed rotating about the inner galaxy with the same center and with a *large* inclination with respect to galaxy’s plane. PRG candidates are objects where these sorts of kinematic followups have not yet been completed. Based on the fraction of galaxies searched that exhibit potential polar rings (0.5%) and the geometric detectability of these structures depending on their sky projection, Whitmore et al. (1990) estimated 5% of all S0 galaxies may be PRGs. Moiseev et al. (2011) used Galaxy Zoo (Lintott et al. 2008) classifications of Sloan Digital Sky Survey (SDSS) images to find 275 PRG candidates, while Reshetnikov & Mosenkov (2019) also mine SDSS to identify 31 new PRG candidates. These searches suggest that, in contrast to milder kinematic misalignments (e.g. García-Ruiz et al. 2002; Ann & Park 2006; Ristea et al. 2022), stellar PRGs are rare within the galaxy population as a whole: their incidence is on the order of $\sim 10^{-3}$ (Reshetnikov et al. 2011), and polar structures around red systems are about twice as common as those around blue systems (Smirnov & Reshetnikov 2022).

It is worth noting that relatively few PRG candidates have been modelled in detail to confirm that they are likely to host polar structures. Moreover such modelling may indicate that the stellar structure is more consistent with being an extreme warp than a truly distinct ring (e.g. Józsa et al. 2009). Such a distinction is largely a matter of semantics given that both extreme symmetric warps, polar rings/disks, and inclined rings/disks are part of the larger continuum of symmetric kinematically misaligned objects. These likely have similar origins and may form an evolutionary sequence (i.e. PRGs and inclined rings may transform into warps; Brook et al. 2008).

Atomic hydrogen (H I) structures exhibiting extreme kinematic misalignments relative to their host galaxies have also been discovered. Many early studies targetted stellar PRGs to look for H I counterparts, finding co-located gas rings (e.g. van Gorkom et al. 1987) or disk (Brook et al. 2008; Džudzar et al. 2021). Similarly, De Rijcke et al. (2013) found a possible H I ring about the FCC046 dwarf ellipti-

cal galaxy in the Fornax cluster, while Bait et al. (2020) found an offset H I ring around the massive quiescent galaxy AGC 203001. Another interesting example is the irregular galaxy NGC 6822, where the gas is coincident with a young stellar disk that is inclined at $\sim 60^\circ$ to an extended spheroid with an older population (Demers et al. 2006; Zhang et al. 2021).

While gas may be found around stellar PRGs during followup observations, there are also systems in which polar H I components are seen without a corresponding stellar counterparts down to SDSS depths. For example, Stanonik et al. (2009) found a single H I disk perpendicular to the stellar disk of the void galaxy SDSS J102819.24+623502.6., while the H I ring of the SB0 galaxy NGC 4262 coincides with a series of UV-bright knots (Buson et al. 2011). While these are individual galaxies, larger H I surveys are also uncovering more objects with single H I components that are misaligned from the stellar structures. Serra et al. (2012) examined the H I content of 166 early-type galaxies from the ATLAS^{3D} survey (Cappellari et al. 2011). They found three galaxies with single-component H I disks that have position angles at $\sim 90^\circ$ to the stellar components. While no stellar counterpart is seen with the H I it is worth noting that the optical data may not yet be deep enough to see such low surface brightness features.

In addition to these single component H I polar structures, there are a number of galaxies where the H I shows multiple components. Schiminovich et al. (2013) observed the elliptical ‘shell’ galaxies Arp 230 and MCG -5-7-1, identifying and kinematically modelling both inner and outer H I components. Translating their inclination and position angle fits for the inner and outer disks suggests that the Arp 230 outer structure is inclined at $\sim 60^\circ$ to the inner disk. For MCG -5-7-1, the inner and outer structures are less distinct kinematically, which may be due to the observations of that galaxy having a lower signal-to-noise ratio (S/N). More recently, Cao et al. (2022) found two galaxies in the Mapping Nearby Galaxies at Apache Point Observatory (MaNGA; Bundy et al. 2015) survey harbouring inner and outer gaseous disks, that are both misaligned from the stellar component, in a sample of 84 galaxies with large dispersions in their gaseous kinematic position angles but with well-measured stellar position angles. In this particular case they use H α observations of the ionized gas rather than H I.

In this paper, we report on two galaxies from the WALLABY Pilot Data Release 1 (PDR1, Westmeier et al. 2022), NGC 4632 and NGC 6156, which we identify to have multiple H I components with symmetric kinematic misalignments. The morphology and kinematics of their H I distributions suggest that these structures plausibly could be polar, a possibility that we explore with perfectly polar kinematic models that we developed to apply to the relatively low resolution and low signal-to-noise observations presented here. Although these models confirm that the anomalous gas in NGC 4632 and NGC 6156 could plausibly be polar, we cannot rule out the possibility of a strong warp (see Sec. 4 for details); we therefore refer to these systems as *potential H I PRGs* throughout. These systems differ from the majority of other systems with gas-rich rings (e.g. van Gorkom et al. 1987; Serra et al. 2012; De Rijcke et al. 2013; Bait et al. 2020), in that the hosts are gas rich late-type galaxies. This expands the study of polar H I structures beyond

the S0 class that typically defines PRGs, but presents the additional challenge of separating the anomalous gas in the ring from that of the underlying H I disk. We carry out this task in an immersive 3D virtual reality environment (Jarrett et al. 2021).

Recent discoveries of polar H I structures are particularly interesting in the context of understanding cosmological galaxy assembly, as simulations suggest that they may result from gas accretion and infall (Khoperskov et al. 2021). This raises the possibility that the incidence of H I-rich rings around nearby galaxies in particular – “H I PRGs” – could constrain this evolutionary process. While a first estimate of the incidence of H I PRGs may be inferred from studies like Serra et al. (2012) and Cao et al. (2022) (although in the case of Cao et al. (2022), the misalignment is seen H α emission, so perhaps gaseous PRGs is more appropriate), the targetted nature of the existing surveys and the lack of consideration of detectability therein implies that the corresponding census is incomplete. Obtaining a true measure of the incidence of H I PRGs requires untargetted H I surveys with sufficient depth, angular resolution and sky coverage to identify them, as well as a framework for assessing H I PRG detectability. The observational piece of this picture will soon be in place with a new generation of widefield surveys that are underway now, such as the Widefield ASKAP L-band Legacy All-sky Blind survey (WALLABY, Koribalski et al. 2020) on the Australian SKA Pathfinder (Johnston et al. 2008; Hotan et al. 2021). In this paper, we leverage the detections of potential H I PRGs NGC 4632 and NGC 6156 in WALLABY PDR1 to develop the first framework for estimating H I PRG detectability from untargetted H I surveys, using both morphological and kinematic information and accounting for geometric and resolution effects.

The paper is laid out as follows. Sec. 2 examines the WALLABY H I observations of NGC 4632 and NGC 6156, and Sec. 3 discusses ancillary optical and mid-infrared (MIR) observations. Section 4 presents an exploration of whether these galaxies are consistent with simple, perfectly polar models using a new formalism that we have developed. Section 5 leverages the untargetted nature of WALLABY to estimate the incidence of H I PRGs given the detectability of the NGC 4632 and NGC 6156 model polar rings determined from mocks at different ring projections and angular resolutions. Finally, Sec. 6 gives our discussion and conclusions. Additionally Appendix A describes attempts at modelling warps and inclined rings, while Appendix B describes the mathematical derivation of the perfectly polar models.

2 WALLABY OBSERVATIONS

WALLABY (Koribalski et al. 2020) is an untargetted Southern Hemisphere survey that will detect the H I gas content of ~ 210000 galaxies (Westmeier et al. 2022) out to $z \sim 0.1$. The survey will cover all of $-60^\circ \leq \text{DEC} \leq -15^\circ$ with some extensions reaching to $\text{DEC} = 10^\circ$. Westmeier et al. (2022) released the PDR1 observations consisting of three fields observed at the full WALLABY sensitivity centered on the Hydra and Norma clusters, and the NGC 4636 group. Each field covers 60 square degrees of the sky constructed from two adjacent tiles, which themselves are composed from two interleaved 36 beam ASKAP footprints, providing a fairly

uniform noise of ~ 1.6 mJy/beam with a beam full-width at half-maximum (FWHM) of $30''$. Once the mosaiced cubes are constructed, the SOFIA source finder (Serra et al. 2015; Westmeier et al. 2021) is used to detect individual H I sources in all fields. The PDR1 catalogue consists of 301 detections in Hydra, 144 detections in Norma, and 147 detections in NGC 4636. The majority of them are marginally resolved, with only 190 having an estimated H I distribution size along the major axis that is wider than 4 beams. In what follows, we define the H I diameter D_{HI} as the major axis extent within which the axisymmetric surface density distribution exceeds $1 M_\odot \text{pc}^{-2}$, measured in $30''$ WALLABY beams.

A visual inspection of PDR1 source datacubes revealed two detections with ring-like H I components that appear to have a very different geometry from that of the inner H I disk: NGC 4632 (WALLABY J124232-000459), and NGC 6156 (WALLABY J163452-603705). H I and optical imaging of these systems are presented in Figures 1–4, and their basic properties are listed in Table 1. The anomalous H I components in both systems are separable from that of the main disks in position-velocity space. We do so for both galaxies using the virtual reality software package iDAVIE¹ (Comrie et al. 2021), designed to explore and interact with spectral imaging and other 3D data sets (Jarrett et al. 2021). iDAVIE’s ‘*paint*’ tool allows direct editing of the cube masks in an immersive 3D environment, which we have used to define masks that separate the anomalous from main disk gas. This is a particularly powerful tool for low resolution, low S/N observations as it allows for adjustments at the individual pixel level while still allowing the user to view the entire cube. However, as the separation is done via visual inspection, some quantities calculated by comparing the two components, such as the mass ratio, are approximations.

In this section, we describe the H I morphologies of NGC 4632 and NGC 6156, both as a whole and separated into main disk and anomalous components. Both here and throughout, we adopt a moment 1 colormap generated using a modified version of the COSMOSCANVAS package². The colormap is designed to evoke the gas kinematics themselves, where the blueshifted gas appears to move ‘out of the page’ and the redshifted gas appears to move ‘into the page’. The colormap also emphasizes differences between gas at velocities slightly above and below the systemic velocity, which is particularly useful in this study.

2.1 NGC 4632

The anomalous H I gas detected by WALLABY in NGC 4632 was first reported in Lee et al. (2022). NGC 4632 is a member of a triplet system with NGC 4666 and NGC 4668 (Sandage & Bedke 1994) and is classified as an SAc galaxy (Ann et al. 2015). Recently Morales et al. (2018) included NGC 4632 in their search for tidal features in a subsample of the S⁴G survey (Sheth et al. 2010; Querejeta et al. 2015) from the *Spitzer* Space Telescope imaging (Werner et al. 2004), and did not find a noticeable tidal feature in the IR imaging. We adopt the Cosmic Flows-III distance to NGC 4632 of 15 Mpc (Tully et al. 2016), placing it considerably more nearby than

¹ <https://idavie.readthedocs.io/>

² <https://github.com/mlarichardson/CosmosCanvas>

estimates from pure Hubble flow ($D \sim 24.6$ Mpc, Westmeier et al. 2022).

The WALLABY detection of NGC 4632 is ~ 10 beams in diameter, making it one of the better-resolved PDR1 sources. Figure 1 shows an overlay of the anomalous component onto imaging taken from the Hyper Suprime-Cam Subaru Strategic Program (HSC-SSP, Aihara et al. 2018), highlighting the mis-alignment of this gas relative to the underlying stellar disk.

Figure 2 shows the 3D projections, the moment 0 and moment 1 maps, and velocity profiles of the H I in NGC 4632 divided into the total, main body, and anomalous gas (left, middle, and right columns). In both the 3D projection and the moment 0 map, the main body of NGC 4632 appears as a cigar-shaped structure in position-velocity space, while the anomalous gas appears as a tilted ring with a significantly different orientation than that of the main body. The ring is less distinct from the main body in the moment 1 map and velocity profile given its sky projection, an issue to which we return in Section 5.

The mask about the main body gas is constructed using iDAVIE to be relatively tight in order to facilitate the kinematic modelling described in Section 4. We find a ratio of main body to anomalous gas mass of $M_{\text{anomalous}}/M_{\text{body}} \sim 0.9$, which may be overestimated due to the tightness of the mask adopted, but the anomalous gas is clearly a significant contribution to the total H I content of NGC 4632.

2.2 NGC 6156

The second potential H I PRG, NGC 6156, has been classified as an SAB(rs)c pec (de Vaucouleurs et al. 1991), but it is important to note that it is located in the Norma cluster near the zone-of-avoidance. Despite the high extinction towards this galaxy, NGC 6156 has been detected in IRAS (Sanders et al. 2003) with a bright IR flux and is therefore a Luminous Infra-Red Galaxy (LIRG).

Figure 3 shows an overview of the WALLABY observations of NGC 6156. In contrast to NGC 4632 in Figure 2, the moment 0 map of the full H I emission for this galaxy shows little sign of anomalous gas, whereas the 3D projection and moment 1 map show an anomalous component roughly perpendicular to the main body in position-velocity space with a bipolar velocity structure. This highlights the importance of examining the full kinematics of the gas distribution to identify anomalous components, which we discuss in the context of polar ring detectability in Section 5.

As with NGC 4632, we use iDAVIE to separate out the main body from the anomalous gas in NGC 6156, and these components are shown in the second and third columns of Figure 3 respectively. However, the resolution and lower S/N of this detection compared to NGC 4632 makes this separation more uncertain. There is a projected spatial overlap between the outer main body and inner anomalous H I in NGC 6156, but the anomalous gas is separated from the main body in velocity space. Given the collisional nature of gas, it is likely separated in Cartesian space as well. It appears that the anomalous component is roughly face-on, given the low line-of-sight velocities in the moment 1 map and single-peaked anomalous H I velocity profile.

Figure 4 shows an overlay of the anomalous H I on a composite $g+r$ -band CTIO DECam image of NGC 6156,

created using the same approach as described for Figure 1. The flux ratio of anomalous to main body H I is $M_{\text{anomalous}}/M_{\text{body}} \sim 1.3$. As with NGC 4632, uncertainties in the mask construction render this mass ratio uncertain, but the anomalous gas clearly contributes a great deal to the total H I mass of NGC 6156.

3 SUPPLEMENTAL DATA

3.1 NGC 4632

The depth of the HSC imaging for NGC 4632 presented in Figure 1 affords a search for low-surface brightness optical features beyond the main disk. Figure 5 shows an exposure time-weighted composite g , r , and z -band HSC image with a logarithmic stretch to highlight the low surface brightness features. A clear ring-like stellar extension is seen in the image stack that is coincident with the southern portion of the anomalous H I shown by the contours in Figure 5, suggesting a common origin. This structure will be studied in detail in future work (Wang et al., in prep). In addition to this faint feature, Figure 1 shows that the stellar disk is more extended to the Southwest than to the Northeast relative to the centre of light.

In addition to the WALLABY and Subaru HSC observations for NGC 4632, we obtained archival custom-built mosaics from the WISE Extended Source Catalogue (WXSC; Jarrett et al. 2013, 2019). The left-hand panel of Figure 6 shows the WISE W1 $3.4 \mu\text{m}$ WXSC observations overlaid with the H I contours of the WALLABY moment 0 data. The W1 flux peak in NGC 4632 is mildly offset to the Southwest, i.e. on the side of the disk minor axis that is more extended in the HSC imaging (Figure 1).

We use the WISE colors and W1 luminosity (Jarrett et al. 2023) to estimate the stellar mass M_* of NGC 4632 and find $\log(M_*/M_\odot) = 9.69 \pm 0.08$, making it somewhat less massive than the Milky Way. This stellar mass coupled with the total H I mass gives a gas fraction ~ 0.3 dex greater than the trend seen in the xGASS galaxies observed in Catinella et al. (2018). We also estimate the star formation rates using the W3 and W4 luminosities (Cluver et al. 2017, see also Cluver et al. 2022, in prep) as $0.73 \pm 0.07 M_\odot \text{yr}^{-1}$, which is well within the star formation main sequence (Figure 7).

3.2 NGC 6156

The high extinction in the direction of NGC 6156 limits the quality of ancillary optical imaging. In the DECam imaging shown in Figure 4, the spiral structure to the South appears more flocculent than that to the North. The WISE W1 WSXC image in Figure 6 shows hints of the structure seen in the optical but with a more extended outer disk, the difference likely arising from the high optical extinction in the region. The WALLABY main body emission appears well-aligned with the W1 emission, with a similar ellipticity.

Following the same procedure as for NGC 4632, we use the different WISE images to estimate $\log(M_*/M_\odot) = 10.75 \pm 0.08$ and $\text{SFR} = 17.60 \pm 1.83 M_\odot \text{yr}^{-1}$ for NGC 6156. Again, the gas fraction, $M_{\text{H I}}/M_*$, is ~ 0.3 dex above the general trend of Catinella et al. (2018), indicating that the galaxy is indeed gas-rich. Moreover, the high star formation



Figure 1. Anomalous H I component of the potential H I PRG NGC 4632, overlaid on a composite *grz* image from the Hyper Suprime-Cam Subaru Strategic Program (HSC-SSP, [Aihara et al. 2018](#)), with the white bar in the bottom-left showing the image size scale. The anomalous gas clearly has a different orientation from that of the stellar disk. The H I intensity map in this figure is created by binning velocity channels together into several individual intensity maps, assigning a colour to each individual map, and blending them into one image. This retains some velocity information while rendering the H I intensity distribution, which we emphasize by using only subtle colours for velocity. Moment 0 and moment 1 maps of the total emission, main body and anomalous H I components of NGC 4632 are shown with linear intensity and velocity scales as well as with coordinate axes in Figure 2.

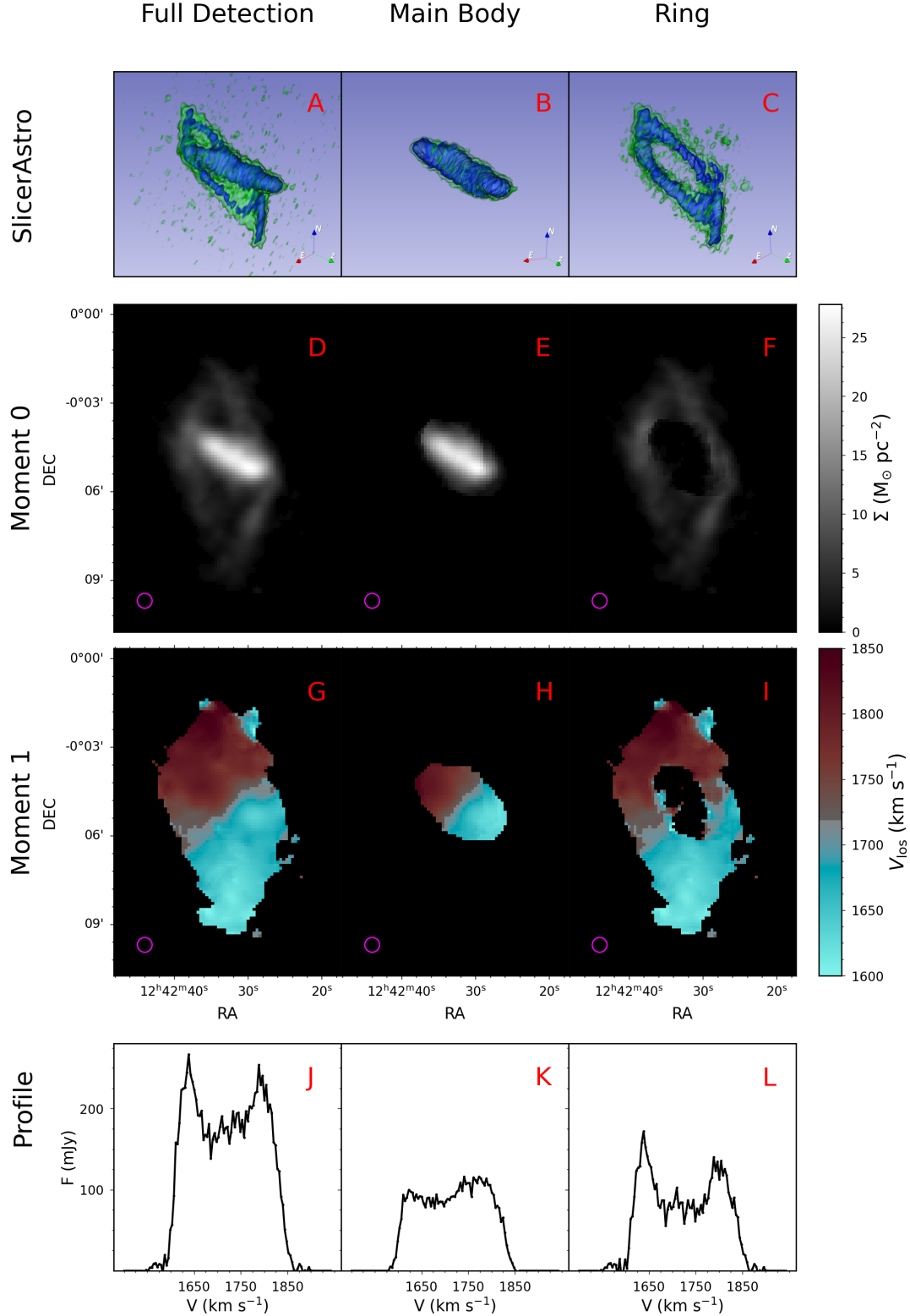


Figure 2. An overview of the WALLABY PDR1 H I detection of NGC 4632. From left to right, the columns show the full detection, the gas associated with the galaxy main body (found using a custom iDAVIE mask), and the anomalous gas. For illustrative purposes, panels A–C in the top row show 3D projections of each component using SLICERASTRO (Punzo et al. 2017). In these panels, the E , N , Z axes correspond to RA, DEC, and V_{los} . Panels D–F (second row) and panels G–I (third row) show moment 0 (panels D–F) and moment 1 (panels G–I) maps, respectively, with the magenta circles denoting the beam FWHM. Finally, panels J–L (bottom row) show the H I profiles for each component.

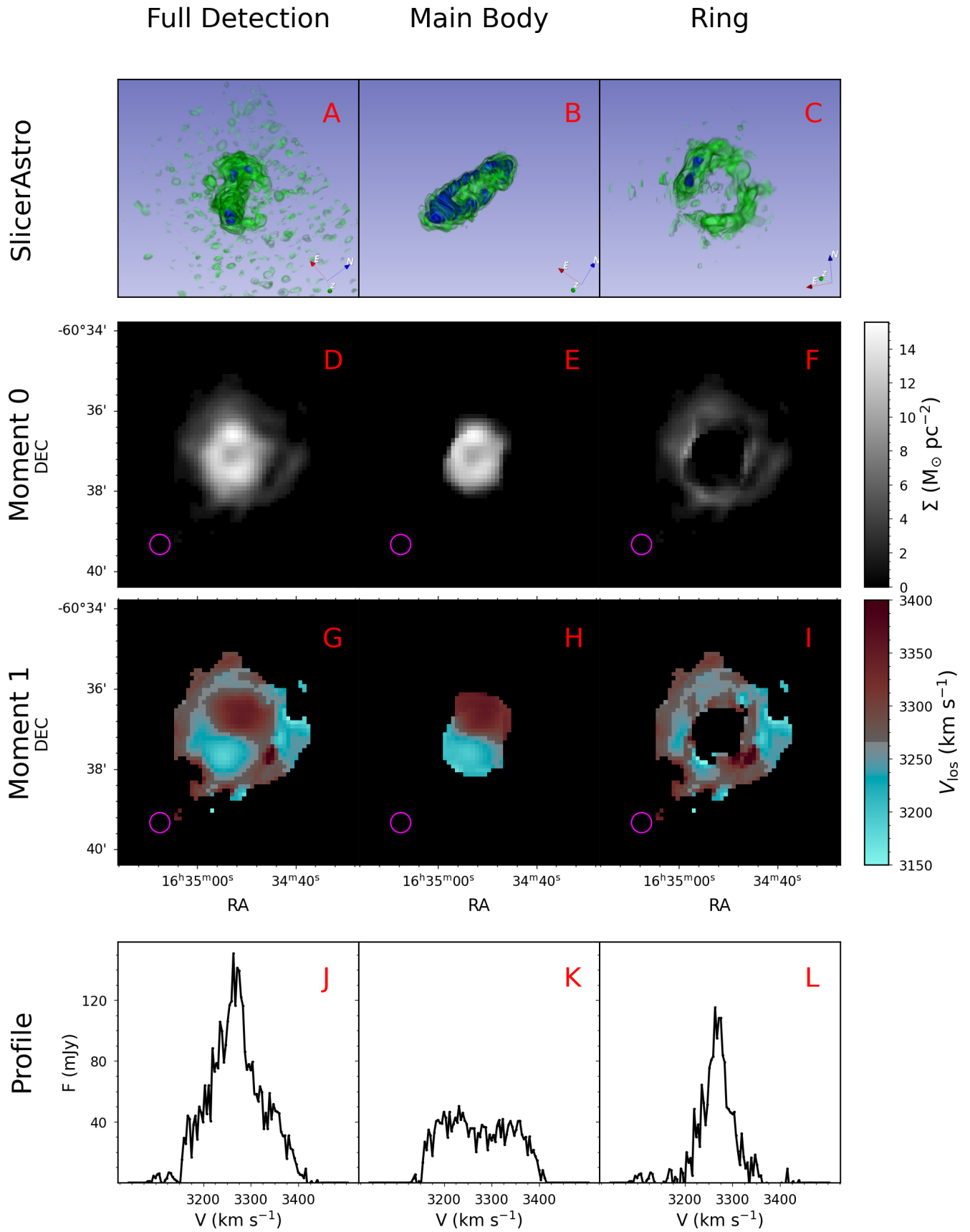


Figure 3. An overview of the WALLABY PDR1 H I detection of NGC 6156. The panels are the same as in Figure 2.

	NGC 4632	NGC 6156
WALLABY Name	WALLABY_J124232-000459	WALLABY_J163452-603705
Type	SAC	SAB(rs)c pec
RA (J2000)	12 ^h 42 ^m 32 ^s ± 5''	16 ^h 34 ^m 50 ^s ± 13''
DEC (J2000)	−0°4′50'' ± 5''	−60°37′2'' ± 9''
V_{sys} (km s ^{−1})	1719 ± 5	3266 ± 15
D (Mpc)	15 ± 2	48 ± 3
H I Flux (Jy km/s)	45.5 ± 0.5	15.3 ± 0.5
log(M_{HI}/M_{\odot})	9.37 ± 0.01	9.92 ± 0.02
log($M_{HI,body}/M_{\odot}$)	~ 9.1	~ 9.5
log($M_{HI,anomalous}/M_{\odot}$)	~ 9.0	~ 9.6
$M_{anomalous}/M_{body}$	~ 0.9	~ 1.3
log(M_{*}/M_{\odot})	9.69 ± 0.08	10.75 ± 0.08
SFR ($M_{\odot}\text{yr}^{-1}$)	0.73 ± 0.07	17.60 ± 1.83

Table 1. The characteristics of the two potential H I PRGs. The center positions and systemic velocities and associated uncertainties are from the kinematic modelling of the main body described in Sec. 4. The total H I flux is drawn from Westmeier et al. (2022) and the distances are from Tully et al. (2016). The H I mass is calculated using the distances and fluxes, while the stellar mass and SFR are calculated from the archival WISE detections as described in Section 3. The uncertainties in the total flux are drawn from Westmeier et al. (2022) and then propagated into M_{HI} . The separation into main body and anomalous H I is done by eye and is rather uncertain (see Sec. 2 for details), and we therefore list approximate values for the corresponding H I masses and ratio.

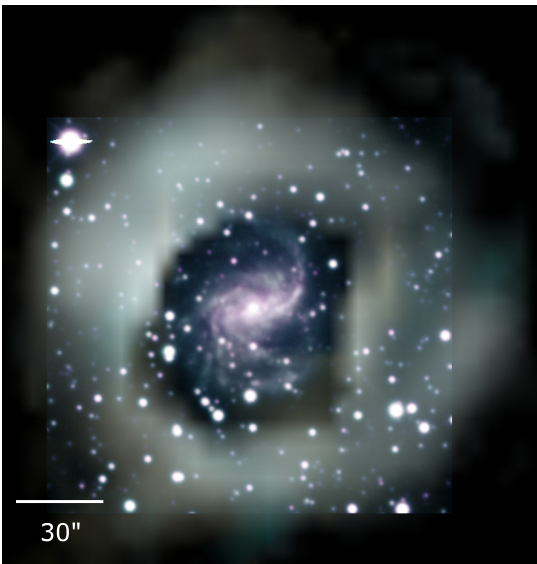


Figure 4. Anomalous H I component of the potential H I PRG NGC 6156, overlaid on a composite *gr* DECam image. The white bar in the bottom-left shows the image size scale. The H I component is rendered in the same manner as in Figure 1. Moment 0 and moment 1 maps of the total emission, main body and anomalous H I components of NGC 6156 are shown with linear intensity and velocity scales as well as with coordinate axes in Figure 3.

rate is above the star forming main sequence (see Figure 7) indicating that the galaxy is currently star bursting, consistent with its bright IRAS emission (Sanders et al. 2003).

4 CONSISTENCY WITH POLAR RINGS

It is clear from Sec. 2 that NGC 4632 and NGC 6156 contain a significant quantity of anomalous gas. It is possible that this anomalous gas is some sort of polar structure (ring or disk), an inclined ring, or a warp. Observationally and in some theoretical models, warps and polar rings may be con-

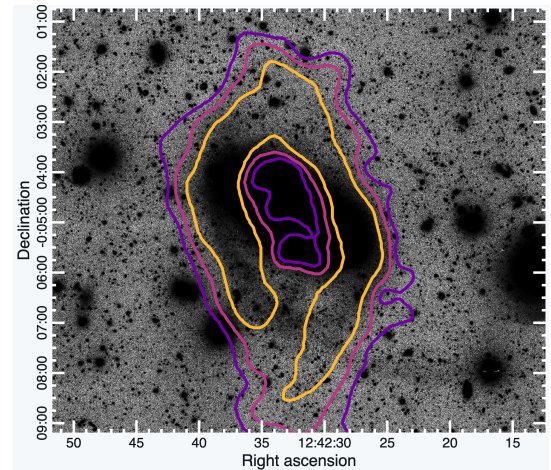


Figure 5. Logarithmically-stretched composite *grz* HSC image of NGC 4632, with anomalous H I component contours overlaid. The purple, pink, and orange H I contours (going from dark to light) are set to 2, 6, and 12 $M_{\odot} \text{pc}^{-2}$ respectively.

sidered as part of the same continuum of kinematically misaligned galaxies. The distinction between an extreme warp or a polar structure is ill-defined, but in general warps exhibit a smooth transition between the main body and the anomalous gas while rings or disks exhibit a sharp discontinuity. Kinematic modelling can distinguish between these different classes of objects, provided that the observations have sufficiently high angular resolution and S/N (Józsa et al. 2009; Arnaboldi et al. 1997).

Unfortunately, our data are of low resolution with a correspondingly low S/N (c.f. Figs. 2 and 3), making the detailed modelling required to distinguish warps from polar rings difficult. We attempt to fit warped models in Appendix A for completeness; only those applied to NGC 4632 converge to solutions, which themselves are inconclusive. In this section, we therefore adopt the more restricted approach as described below.

There are reasons to posit that NGC 4642 and

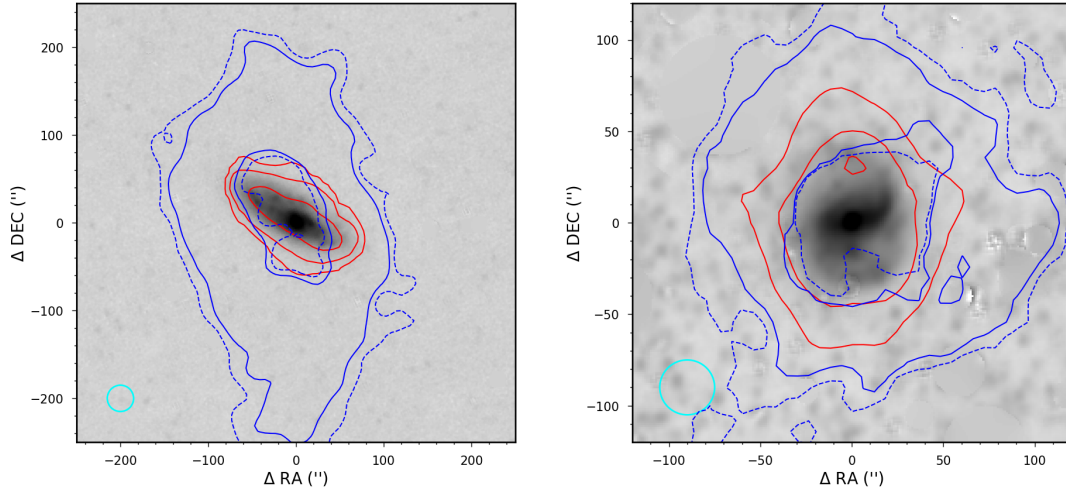


Figure 6. WISE W1 $3.4\mu\text{m}$ WSXC images of NGC 4632 (left panel) and NGC 6156 (right panel) with the H I gas overlaid. In both panels the greyscale WISE images are plotted in logarithmic units, while the main body and anomalous H I are shown as red and blue contours, respectively. For NGC 4632 in the left panel, the red contours are at $(5, 10, 20) M_{\odot} \text{pc}^{-2}$ and the dashed and solid blue contours are at $(2, 6) M_{\odot} \text{pc}^{-2}$. For NGC 6156 in the right panel, the red and blue contour levels are $(5, 10, 15) M_{\odot} \text{pc}^{-2}$ and $(0.5, 1.5) M_{\odot} \text{pc}^{-2}$ respectively. The cyan circles in the bottom-left corner of both panels show the WALLABY beam FWHM, and coordinates in both panels are given relative to the centre points listed in Table 1.

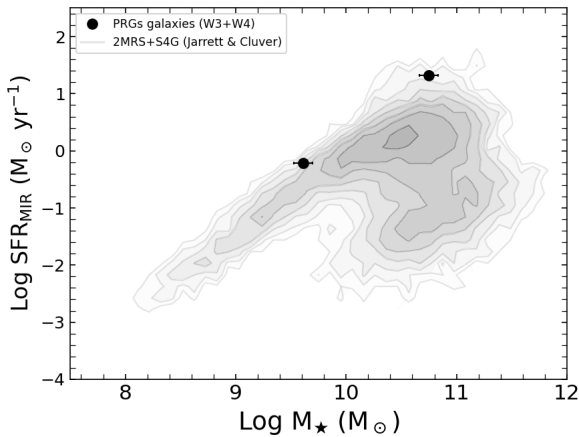


Figure 7. The star formation rate as a function of stellar mass, both derived from WISE mid-infrared measurements. The two potential H I PRGs are indicated with points and estimated uncertainties, where NGC 4632 is at lower mass and with an SFR that is consistent with normal field galaxies, and NGC 6156 has a higher mass and excess SFR indicating a starburst phase. For comparison purposes, the contours and greyscale represent a large sample of nearby bright galaxies from the WISE Extended Source Catalogue (Jarrett et al. 2013, 2019).

NGC 6156 are H I PRGs. Firstly, the anomalous gas seen in NGC 4632 appears to be well separated from the main body, strongly suggesting a ring rather than a warped disk. This is reinforced by the faint stellar ring in the HSC imaging is coincident with the southern portion of the anomalous gas (Fig. 1). Moving to NGC 6156, the anomalous gas appears to be mostly face-on, but the hint of rotation implies a position angle that is $\sim 180^\circ$ to the main body. Beyond these morphological clues, another reason to suspect that the anomalous gas is polar is that PRGs are far more stable and long-lived than inclined rings or extreme warps, on

which the torque from the main disk are strong (Bournaud & Combes 2003; Brook et al. 2008). As such, if the anomalous gas has an extreme morphology, it is more likely to be a polar ring than a ring or disk at an intermediate angle.

We therefore consider whether or not perfectly polar models of the anomalous gas can reproduce the key features observed in the H I content of NGC 4632 and NGC 6156. We adopt a tilted-ring (TR) approach, which is widely used to kinematically model galaxies. Section 4.1 describes TR modelling in general, while Sec. 4.2 describes our method of perfectly polar ring modelling. Sections 4.3 and 4.4 present our models for NGC 4632 and NGC 6156 respectively.

4.1 General Tilted Ring Modelling

The basic ideas of TR modelling were proposed in Warner et al. (1973) and Rogstad et al. (1974), and since that time it has become one of the most widely used methods of generating kinematic models of H I galaxies. There are a variety of 2D TR modelling codes like ROTCUR (Begeman 1989; van der Hulst et al. 1992) and 2DBAT (Oh et al. 2018) that fit velocity maps (moment 1 maps). More recently TR modelling methods have been developed to fit 3D data cubes directly. Some of the more common codes are TIRIFIC (Józsa et al. 2007), 3DBAROLO (Di Teodoro & Fraternali 2015), and FAT (Kamphuis et al. 2015), but there are a number of other codes available as well (e.g. KINMS, Davis et al. 2013 and GBKFIT, Bekiaris et al. 2016).

A TR model is described by a set of rings, which in turn are characterized by a set of geometric and kinematic parameters. In 3D methods, mock observations are generated and compared to observations. These mock observations are made by first filling the rings with tracer particles and placing them in a data cube. Then the mock cube is convolved with an appropriate beam and frequency response function so that it may be directly compared to the data. The best fitting model is typically found by repeating this process and

either minimizing some goodness of fit statistic or exploring the parameter space using Bayesian statistics. Below, we describe a TR model in which the anomalous gas is a perfectly polar ring, which has many fewer free parameters than a generalized TR model in which the disk is allowed to warp (Józsa et al. 2009; Arnaboldi et al. 1997).

4.2 Perfectly Polar Ring Modelling

In a perfectly polar model, the ring has a sky-plane inclination, i_r , and position angle, PA_r , such that, when rotated back to the galaxy plane using the main body inclination, i_g , and position angle, PA_g , the ring's inclination with respect to the plane of the galaxy, $i_{r,g}$ will be 90° . To ensure this orientation we have developed a formalism relating the galaxy-ring plane geometry to the projected geometry.

The full derivation of the polar ring geometry is found in Appendix B. In this formalism, we have defined the angle that the ring makes with the approaching side of the galaxy as β . This can be seen in the left-hand panel of Figure 8, which shows a sketch of a polar ring system in galaxy plane coordinates (left) and sky plane coordinates (right). Given β and a galaxy's observed inclination i_g and position angle PA_g , the ring's inclination i_r and position angle PA_r can be calculated. Defining $\theta = PA + 90^\circ$ for simplicity, and setting $\theta_g = 0^\circ$, the inclination and position angle of a circular polar ring is

$$\cos(i_r) = -\sin(i_g) \cos(\beta), \quad (1)$$

$$\tan(\theta_r) = \frac{\sin(\beta)}{\cos(\beta) \cos(i_g)}. \quad (2)$$

Then, for any given galaxy position angle, the ring's position angle is

$$PA_r = \theta_r - 90^\circ + PA_g. \quad (3)$$

One thing to note is that in Eq. 2, the β terms have not been simplified to $\tan(\beta)$. This is done to allow the range of θ_r to span $0^\circ \leq \theta_r \leq 360^\circ$.

The relation between the observed galaxy geometry and β to the ring's observed geometry allows for a relatively straightforward approach to kinematically model PRGs. First, it is necessary to construct a 'tight' mask that isolates the gas belonging to the host galaxy from the anomalous gas, and we use the iDAVIE masks described in Sec. 2 for this purpose. The next step is to kinematically model the galaxy body to determine its geometry and approximate outer rotation of the galaxy. The geometry is necessary for the polar ring modelling, and the rotation velocity can be used as a consistency check for the modelled ring. We used the 3DBAROLO³ code (Di Teodoro & Fraternali 2015) to generate the galaxy model as it is fast and can be run with a user supplied mask. This ensures that the model is only applied to the gas contained within the 'tight' mask. Given the low resolution and S/N , during this step the galaxy body is modelled as a 'flat' disk with a constant inclination and position angle. Following Deg et al. (2022), we fit 2 rings per beam. Finally, we model the anomalous gas as a perfectly

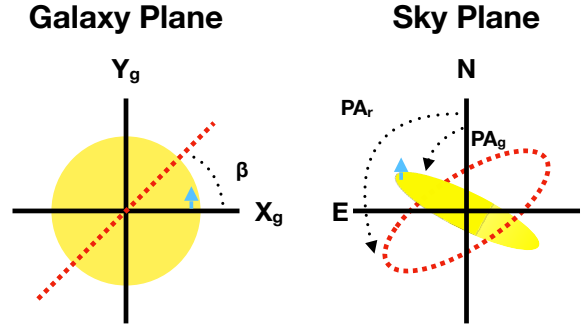


Figure 8. A sketch of a PRG orientation. The yellow circle/oval represents the host galaxy in galaxy plane coordinates (left) and sky plane coordinates (right) while the red dashed line/oval represents the polar structure. In the galaxy plane coordinates, (x_g, y_g) , the positive x_g axis is aligned with the approaching side of the galaxy, represented by the blue arrow in both panels. The angle of the polar ring with respect to the x_g axis is β , which, when coupled with the galaxy's inclination, i_g and position angle, PA_g , uniquely determines the ring's inclination, i_r , and position angle, PA_r , in the sky plane.

polar ring. For simplicity we treat the gas as single ring with three free parameters, β , v_{rot} , and Σ (the ring surface density). This is a limited enough number of free parameters that they can be explored using a basic grid search. To be clear, this step involves comparing the combined ring plus galaxy model to the SOFIA-masked datacube.

4.3 NGC 4632

Armed with the 'tight' mask for NGC 4632, we are able to proceed with the modelling. An additional difficulty in the TR modelling of the galaxy is the importance of the initial inclination estimate. In 3DBAROLO the code will either estimate the TR geometric parameters (position angle and inclination) from the observed moment maps or the user can supply estimates. In low resolution, low S/N observations, 3DBAROLO tends to find final models with very similar parameters to those initial estimates due to the flatness of the likelihood surface. In fact, we find that 3DBAROLO is able to produce acceptable fits for initial estimates of $i_g \geq 55^\circ$. The obvious choice is to select the optical inclination as the initial estimate ($\sim 65^\circ$ based on the Subaru HSC images). But, a secondary problem arrives at high inclinations. As the galaxy becomes more edge-on, Eq. 2 shows that the difference between the galactic position angle and the ring position angle increases. Supplying 3DBAROLO with an initial estimate of $i_g = 65^\circ$ yields a final model with $i_g = 67^\circ$. Such an inclination for the galaxy body causes ring models to have too large of a difference in position angles between the galaxy and the ring to match the observations. In order to obtain a position angle difference similar to that seen in the upper right panel of Figure 2, we chose an initial estimate of $i_g = 60^\circ$ for 3DBAROLO, which yields a final galaxy body model with $i_g = 62.5^\circ$.

With the galaxy body modelled, it is then possible to model the polar ring using a different set of software than

³ <https://editeodoro.github.io/Bbarolo/>

3DBAROLO . MCGSUITE⁴ (Mock Cube Generator Suite; Lewis 2019, Spekkens et al. in prep) is a code that generates standalone TR models from either scaling relations or directly from a set of ring parameters. We model the polar ring by searching the relevant TR parameters and using MCGSUITE to produce mock data cubes that can be compared to the observed data. To get the orientation, rotation speed, and surface density, a grid search of β , v_{rot} , and Σ is performed. The MCGSUITE realization of each full model (body + ring) is then compared to the SOFIA-masked data. Figure 9 shows the final best fitting model, as determined by having the lowest χ^2 value during the mock cube - observation comparison. This model has $\beta = 335^\circ \pm 5^\circ$.

Figure 9 illustrates that the best-fitting model reproduces some of the key features in the NGC 4632 H I detection: the velocity map shows the dual peaks seen in the data. In addition, the difference between the main body position angle and the ring position angle broadly agrees with the observed structure. Nonetheless, there are also differences between the model and the data, such as the sharpness of the transition between the galaxy body and ring region and the inclinations of the main body and ring. It is possible that these differences imply that the ring that is not perfectly polar, but our attempt a modelling such as structure is not a better fit to the data on the whole (see Appendix A). Given that that the perfectly polar model reproduces key features of the observations (a ring like structure with a similar velocity map), it is reasonable to conclude that NGC 4632 is indeed plausibly an H I PRG.

4.4 NGC 6156

NGC 6156 is analyzed using the same procedure as NGC 4632. The ‘tight’ body mask is input into 3DBAROLO and the galaxy body is modelled. As with NGC 4632, supplying an initial estimate for the inclination is critical. The optical observations seen in Fig. 4 as well as the images of NGC 6156 obtained in the Carnegie-Irvine Galaxy Survey (CGS, Ho et al. 2011), suggest that the galaxy ($\sim 40^\circ$). This is consistent with aspect ratio of the H I moment 0 map in Fig. 3E, but inconsistent with the degree of rotation seen in the moment 0 map of Fig. 3H. The WISE image in Figure 6, which we expect to more reliably trace the disk geometry in this high-extinction region, has a morphology that appears more inclined than the optical image and more consistent with the main body H I velocity.

Given the moment 1 map of the galaxy main body and the morphology of the anomalous gas as well as the optical morphology, we provide 3DBAROLO with an initial inclination estimate of $i_g = 50^\circ$, yielding a galaxy model with $i_g = 51^\circ$. NGC 6156 is an even lower resolution and S/N detection than NGC 4632. Thus the small shift from the initial inclination estimate is unsurprising given flatness of the likelihood surface. Given the question of the inclination, we did attempt to model the galaxy using a 40° initial estimate for the main body. However, this model yielded a ring that is even more inclined, with lower rotation velocity, in poorer agreement with the data than the model adopted below.

With the main body model fit from 3DBAROLO the

same grid-based search of β , v_{rot} , and Σ can be done for the ring. As with NGC 4632, 3D realizations of each body+ring model are made using MCGSUITE and the SOFIA-masked observed data cube is compared with these realizations to find the best fit. Figure 10 shows the best fitting model for NGC 6156, which has $\beta = 153^\circ \pm 5^\circ$.

Figure 10 shows that the best-fitting perfectly polar model for NGC 6156 produces a moment 1 map with a similar velocity structure to the data. However, model moment 0 map has a ring that is more distinct, more inclined, and at a somewhat different position angle from the observed gas. Moreover, the low ring velocity relative to the outermost point of the galaxy’s rotation curve raises the question of whether or not it is dynamically stable. These may be indications that the anomalous gas is better described by a warped disk or a ring with $i_{r,g} \neq 90^\circ$ than a polar ring. However, the warped disk models that we attempted to apply to these data did not converge to a solution (see Appendix A), precluding further investigations in this regard until higher-resolution and S/N data are available. Thus while the perfectly polar models of NGC 6156 do exhibit differences from the data, it remains possible that the anomalous gas is a polar structure and an alternate model could not be found. We therefore consider NGC 6156 to be a plausible H I PRG given the quality of the available data.

5 POLAR RING DETECTABILITY IN WALLABY

The detection of two potential H I PRGs in the WALLABY pilot fields is exciting and challenging as they were unexpected. Reshetnikov et al. (2011) estimated the incidence rate of PRGs, f_i , in the local Universe to be $\sim 1/1000$. If the two are indeed H I PRGs, then given the ~ 200 PDR1 detections that are resolved by more than 4 beams is certainly inconsistent with the canonical rate. However, hints of a higher incidence rate for H I PRGs are seen in Serra et al. (2012), as well as in the ionized gas study of Cao et al. (2022). These both show incidence rates closer to 1%, but they are also both targetted surveys, which makes an inference of the true incidence rate much more difficult due to their selection functions. As an untargetted survey, future WALLABY data releases will certainly contain enough detections to determine if there is indeed a higher incidence rate of H I PRGs.

Given the untargetted observing approach for WALLABY, the incidence rate of H I PRGs in PDR1 can be estimated from the two potential H I PRGs that were identified using a relatively simple process. Firstly, detecting a PRG must depend on the geometry of the system and the resolution of the galaxies. That is, there is a geometric detection rate $f_g(b)$ where b is the resolution of the galaxy in beams. Then the number of detected PRGs should be

$$N_{\text{detected}} = f_i \int f_g(b)N(b)db, \quad (4)$$

where N_{detected} is the number of detected H I PRGs, b is the resolution of the galaxies, and $N(b)$ is the number of galaxies at a given resolution. We note that if NGC 4632 and NGC 6156 harbour strong warps instead of true H I PRGs, the incidence rate we estimate nonetheless applies to these extreme kinematically distinct components.

⁴ <https://github.com/CIRADA-Tools/MCGSuite>

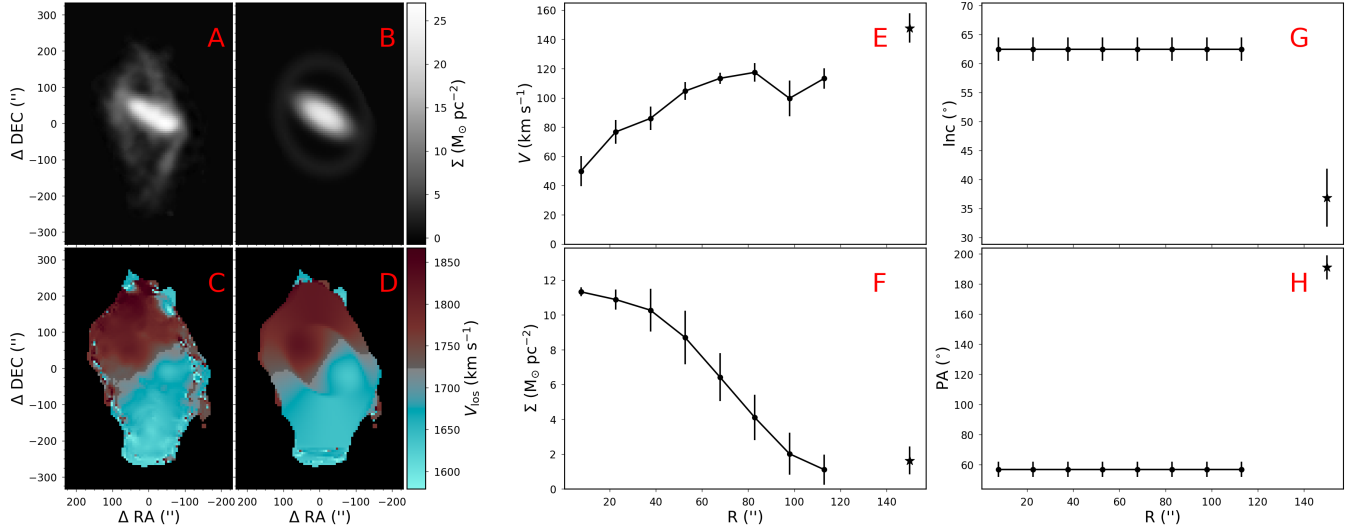


Figure 9. The best fitting perfectly polar ring model of NGC 4632. The moment 0 maps of the galaxy and the model are shown in panels A and B respectively, while the moment 1 maps are shown in panels C and D. The velocity scale in panels C and D is centered at the systemic velocity of the warped 3DBAROLO model. The rotation curve, deprojected surface density, inclination, and position angle profiles are shown in panels E-H respectively. The polar ring parameters are indicated by stars and are the last radial point in each of the right-hand panels. As with Figs. 2 and 3, the moment 0 maps use a linear stretch which explains the differing spatial extents of the moment 0 and moment 1 maps.

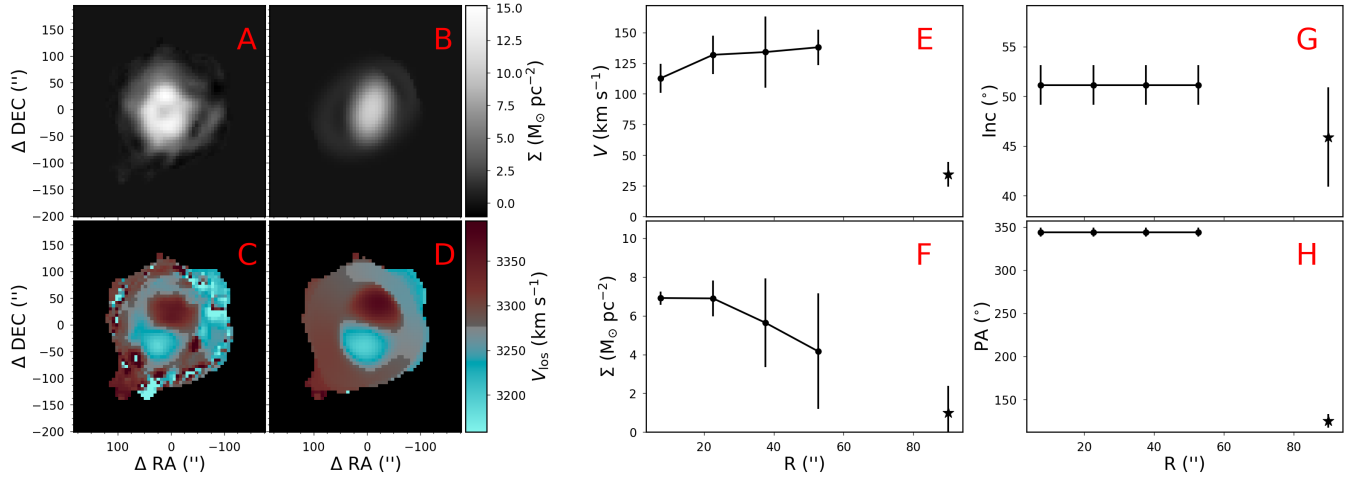


Figure 10. The best fitting perfectly polar ring model of NGC 6156. The panels are the same as in Figure 9.

In order to estimate f_i , it is first necessary to quantify $f_g(b)$. To understand the dependence of HI PRG detectability on geometry and resolution, we generated a suite of mock PRG cubes based on our best fitting NGC 4632 and NGC 6156 models using MCGSUITE. The suite consists of 49 cubes for each model at resolutions of 3, 4, 6, 8, and 10 beams across for a total of 490 mock observations. These cubes span a range of main body inclinations between 0° and 90° and β values between 0° and 180° . Each cube is generated with a noise of 1.6 mJy/beam, matching them to WALLABY. In order to mimic a WALLABY analysis, SoFIA-2 is run on the cubelets to generate a mask. We then visually examined each moment 0 and moment 1 map individually to determine if a signature of a polar ring is

clearly apparent. If the feature can possibly be mistaken for noise, we do not count it in the determination of $f_g(b)$. This determination is subjective, so the calculation of $f_g(b)$ from these maps should be considered as an approximation.

Figures 11 and 12 show the moment 0 and moment 1 maps for the 10 beam resolution NGC 4632 models. The moment 0 panels are shown using the same brightness scale for all panels to show the difference that the inclination makes in the detectability. Similarly, a linear stretch is used for the brightness as this is the typical stretch used when examining many galaxies in a large survey to find interesting outliers, like PRGs. At this resolution, which is roughly the observed resolution of NGC 4632, all orientations in the moment 0 maps show a clear ring structure except perhaps for the

$\beta = 0^\circ$, $i_g = 45^\circ$ panel. For the moment 1 maps in Figure 12, the situation is similar, with most orientations showing a clear sign of a polar ring. However, in the $\beta = 0^\circ$, $i_g = 30^\circ$ and 45° panels, the velocity structure of the polar ring and main disk are orientated such that the polar ring signature is hidden.

A more complicated picture emerges when looking at the NGC 6156 models at 6 beams across shown in Figs. 13 and 14. While the ring is clear in the low inclination panels of Fig. 13, as well as the $\beta = 90^\circ$ panels, at intermediate inclinations the low and high β orientations do not indicate the presence of a polar ring. It is worth noting here that the PRG candidate shown in Figure 1 of Nishimura et al. (2022) bears a striking resemblance to the $i_g = 0^\circ$ moment 0 maps. Moving to the moment 1 maps, a clear polar ring signature is seen in most of the high inclination models. The presence of a rotating disk surrounded by low rotation gas seen in many of the panels is a typical polar ring signature that may not always be appreciated when examining velocity maps. It is in fact this signature that suggested that NGC 6156 is a PRG initially.

An interesting point to note about the 6 beam resolution models is that the moment 0 and moment 1 maps are complementary. At intermediate resolutions, the orientations where the ring is most easily detected in the moment 0 maps are where the velocity maps provide little indication of a ring structure. Similarly, where the moment 1 maps easily see polar rings are the orientations where the moment 0 maps provide less information. This complementarity may allow WALLABY and other interferometric studies to detect many more PRGs than previous works (provided the observations are of sufficient resolution).

While the NGC 4632 and 6156 models are significantly different, a key reason for the lower detectability in Figs. 13-14 compared to Figs. 11-12 is the resolution. To highlight this effect, Figure 15 shows the moment maps for a single geometry of the NGC 4632 model (top rows) and NGC 6156 model (bottom rows) at different resolutions. In both cases, at 3 beams across no polar features can be detected and at 10 beams across the polar ring is clearly detected.

For the purposes of quantifying $f_g(b)$ using the full suite of models, if a polar ring feature is identifiable in either the moment 0 or moment 1 map of a particular model, then we consider that PRG model detectable. The bottom row of Figure 16 shows $f_g(b)$ for the NGC 4632 model (red lines) and NGC 6156 model (blue lines). An interesting trend seen is that, at low resolutions, polar ring features are more easily detected in the moment 1 maps, but at high resolutions they are more easily seen in the moment 0 maps. In both models, at 10 beams across $f_g \sim 1$, while at 3 beams across $f_g \sim 0$.

To obtain a total detectability fraction at a given resolution, the NGC 4632 and NGC 6156 detectability fractions are averaged together. And to apply this at any resolution, we applied a spline fit to the points. The full curve for $f_g(b)$ is shown as the black line in the bottom row of Figure 16.

Armed with a $f_g(b)$, it is possible to estimate the incidence of PRGs in WALLABY PDR1. Rearranging and discretizing Eq. 4 gives

$$f_i = \frac{N_{\text{detected}}}{\sum_b f_g(b)N(b)}. \quad (5)$$

The upper row of Figure 16 shows $N(b)$ of the WALLABY

PDR1 detections, while the bottom row shows $f_g(b)$, allowing an incidence rate to be calculated relatively easily. Using $N_{\text{detected}} = 2$, $f_i \approx 2\%$, which implies that there are approximately 8 PRGs among the 592 galaxies in WALLABY PDR1, despite only 2 being detected. In order to estimate the uncertainty on f_i , we repeated the calculation using $N_{\text{detected}} = 1$ and $N_{\text{detected}} = 3$, yielding $f_{i,\text{low}} \approx 1\%$ and $f_{i,\text{high}} \approx 3\%$ respectively.

This detection rate is a simple approximation based on a number of assumptions that may prove incorrect. The biggest source of error is whether our potential H I PRGs are in fact extreme warps. This is perhaps unlikely for NGC 4632, which would require a fairly extreme warp to reproduce the morphology of the H I but it is certainly possible for NGC 6156. Additionally, our geometric detection analysis is based on visual classifications that are certainly subjective. Moreover, we have not explored the effects of confusion due to the warps that are present in nature. Given this, our high detection rate should be taken as an upper limit on the occurrence of PRGs in WALLABY PDR1.

6 CONCLUSIONS

Using H I alone, we have detected 2 potential H I PRGs in the WALLABY pilot fields, NGC 4632 and NGC 6156. NGC 4632 shows a clear ring structure in the moment 0 map, while NGC 6156 shows a characteristic ring pattern in the velocity map.

Once the existence of the anomalous gas was recognized in the moment maps, we investigated the plausibility of this gas being consistent with a polar ring. To that end, we first separated that anomalous gas from the host galaxy's gas using the iDAVIE VR interactive tool. This allowed for the construction of kinematic models for the host galaxies using 3DBAROLO. We then developed a formalism relating the projected inclination and position angle of a polar ring to the host galaxy's inclination, position angle, and the angle the ring makes with respect to the approaching side of the galaxy. This allowed the exploration of perfectly polar models to find reasonable fits to the data using MCGSUITE.

The kinematic model fit for NGC 4632 is significantly better than the fit for NGC 6156, but it is not perfect. The model moment 0 map contains more of the features seen in the observations compared to the NGC 6156 model and observations. However, our perfectly polar models are very strict and do not encompass the full range of PRG's seen in nature. Polar structures may be slightly elliptical and have inclinations from the galaxy body in the range $75^\circ \geq i_{r,g} \geq 90^\circ$. Exploring these parameters will likely yield much better fits to the data and comparing those models to those of extreme warps will help to confirm whether NGC 4632 is indeed a PRG. At this point, we argue that NGC 4632 is a potential H I PRG until such sophisticated modelling and comparisons to deeper observations are completed.

For the second galaxy in our study, the model fit for NGC 6156 represents a bigger challenge. The lower resolution and S/N of NGC 6156 causes the modelling and interpretation of the anomalous gas to be more ambiguous. The likely orientation of the ring structure means that the polar ring signature appears in the moment 1 map as a rotating disk surrounded by low-rotation gas. While the rotating disk

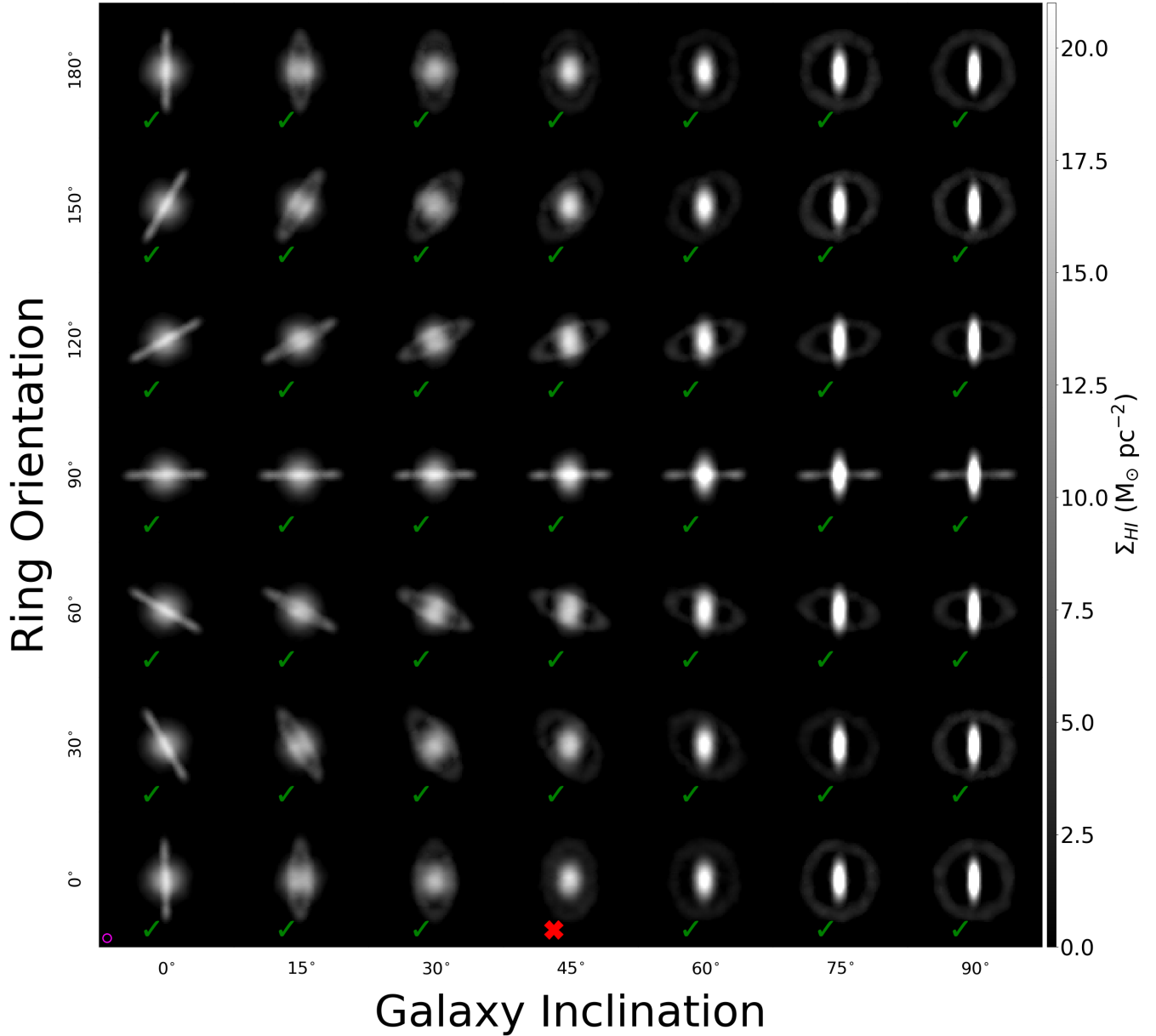


Figure 11. Moment 0 maps computed from different projections of the best fitting H I PRG model for NGC 4632, where the observed geometric parameters β (y-axis) and i_g (x-axis) are varied. These models are built to have resolutions of 10 beams across, which is consistent with observations of NGC 4632. The small magenta circle represents the beam size. The noise level in each model cube is 1.6 mJy/beam, which is consistent with WALLABY. The green checkmarks and show models that are recognizable as PRGs from the moment 0 map, whereas the red x denotes the model that would not be recognizable.

can be clearly separated from the anomalous gas, the kinematic model is difficult to construct. The low S/N of the observations means that goodness-of-fit surface is quite flat, which makes distinguishing good fits from poor fits fairly difficult. Nonetheless, we are able to generate a model with a similar polar ring signature in the moment 1 map as observed, although this model does have an abnormally low rotation velocity for the ring. Like NGC 4632, we expect that a great improvement in the fitting can be made in future work by relaxing the circular and polarity assumptions. In particular, slight deviations from polarity will allow the model ring to be more face-on, which will in turn lead to a

higher model rotation velocity. Given the starbursting nature of NGC 6156 as well as its status as a LIRG, it will be important to explore alternate explanations for the anomalous gas seen in WALLABY PDR1. It may have been generated via (supernovae) outflows or some accretion event that would produce a warp rather than a ring. Given the importance of the galaxy inclination for the PRG interpretation coupled with the more face-on appearance of the stars, an investigation into the possibility of the gas being a warp is critical. However, given the low S/N and resolution of this data, untangling the full morphology of the gas will require both greater sensitivity and resolution. Nonetheless, the reg-

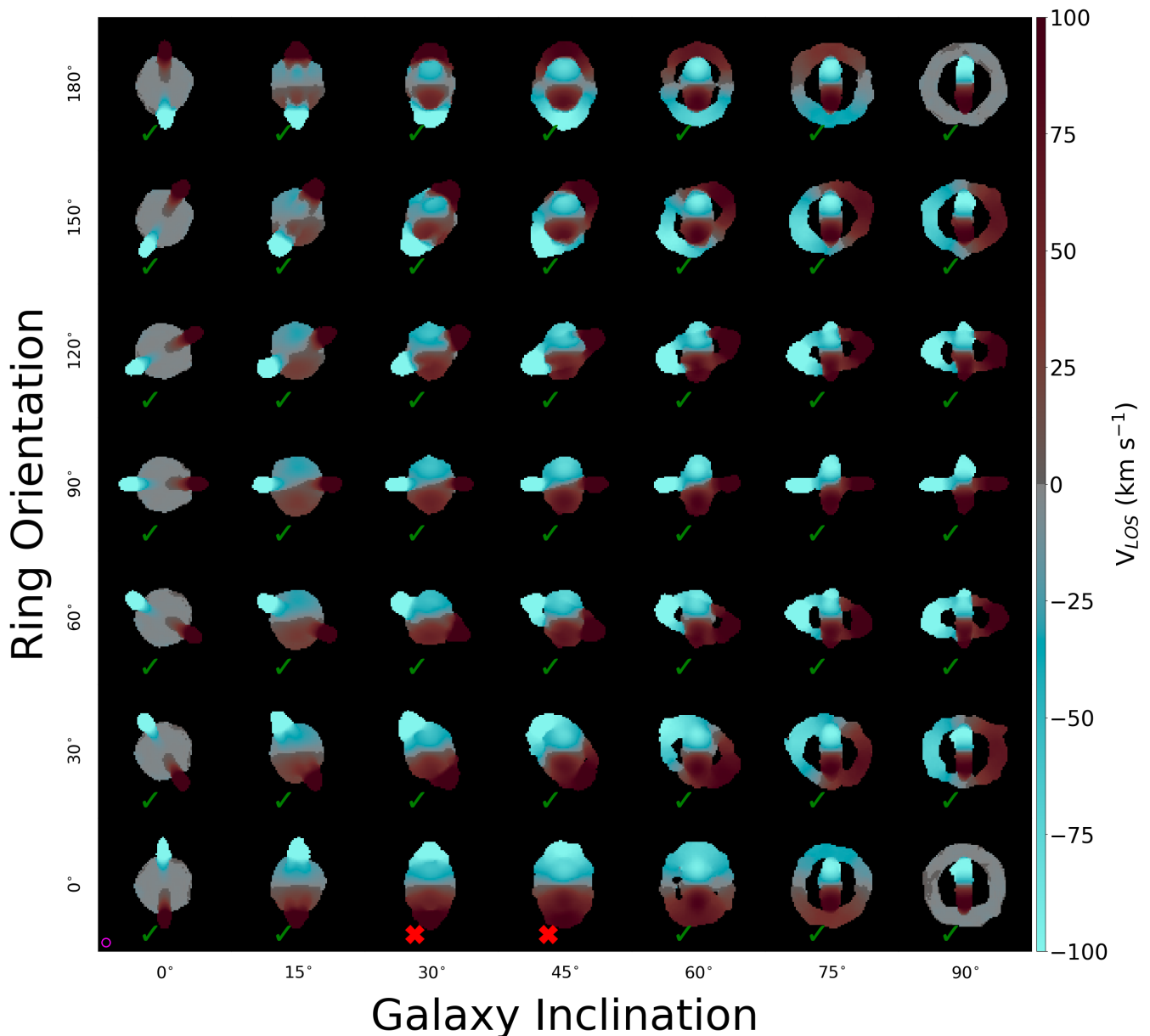


Figure 12. Same as Figure 11, but for the moment 1 maps of different projections of the best fitting H I PRG model of NGC 4632 at a 10 beam resolution.

ular structure of the anomalous gas as well as our ability to reproduce the salient features of the moment 1 map using our rudimentary model (namely the rotating disk signature surrounded by apparently face on gas) suggest that it is possible that NGC 6156 is a PRG, and that it should be considered a potential H I PRG until deeper observations are available.

Finally, we explored the detectability of PRGs in WALLABY by generating identical models with different observed geometries. At low resolutions, it is nearly impossible to detect polar rings, while at high resolutions, PRGs are easily detected in either the moment 0 or moment 1 maps. Combining this with the distribution of WALLABY PDR1 galaxy resolutions allows the estimation of the incidence rate of PRGs. We find $\sim 1\% \leq f_i \leq 3\%$, which

is significantly higher than the canonical rate of 0.1% as measured in Reshetnikov et al. (2011). Our rate for multi-component H I PRGs is in line with the incidence rate seen by Serra et al. (2012), who found 3 PRGs around early type galaxies out of 166 observations. It is worth noting here that we have not yet investigated whether there are any WALLABY detections where single component H I detections are polar to stellar observations. This rate is also similar to the rate of misaligned multi-component gas seen in Cao et al. (2022).

There are reasons to suspect that PRGs in general, and H I PRGs in particular, are more common than previous stellar studies have suggested. Firstly, the detection of stellar polar rings can be difficult due to their low surface brightness. For instance, the faint overdensity detected

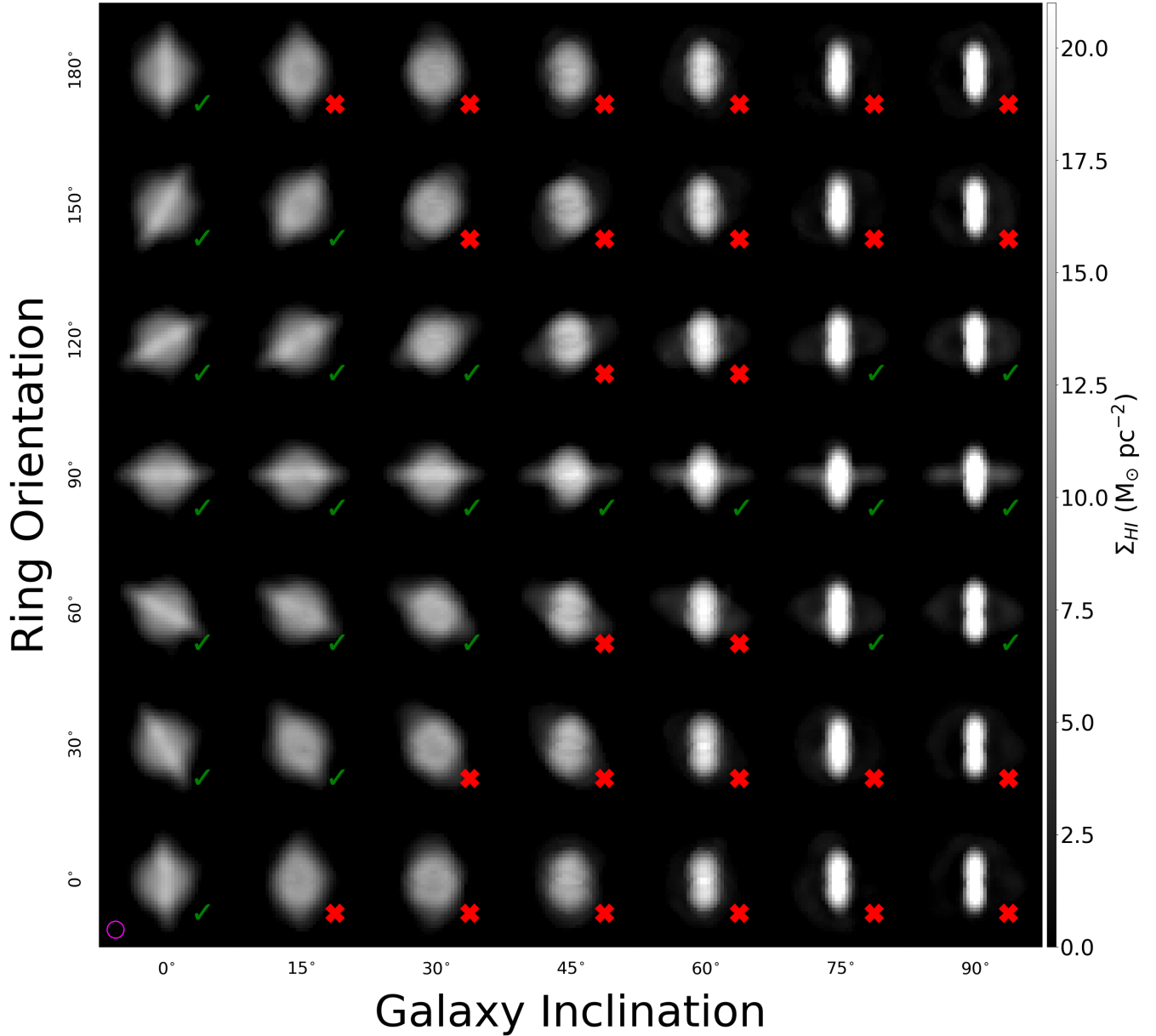


Figure 13. Same as Figure 11, but but for the moment 0 maps of different projections of the best fitting H I PRG model of NGC 6156 at a 6 beam resolution.

around NGC 4632 in Figure 5 is near the noise limit. H I gas has a much smaller dynamical range of surface brightnesses, making it easier to detect with new sensitive arrays. Additionally, the interferometric nature of the WALLABY H I provides the velocity structure which is where the key indications of NGC 6156 being a potential H I PRG are found. Moreover, given that these two potential H I PRGs are found in H I it is possible that H I rings have different formation mechanisms than stellar rings. It is worth noting here that most optical PRGs have been found around S0/E galaxies, while these structures are around spirals. This might be due to a selection bias in detecting PRGs, or it may be a signature of a different origin. Uncovering a larger sample of PRGs will help to determine whether there is real dependence on the host morphology for PRGs.

One other potential reason for the increased incidence of potential H I PRGs in WALLABY PDR1 is the environment. The PDR1 fields were targeted to relatively nearby clusters and groups. Moreover, the NGC 4632 and NGC 6156 are at the outskirts of a massive cluster and group respectively. These environments have frequent tidal interactions and gas-rich mergers (relative to field galaxies), and both of these have the potential to generate PRGs. Moving to the future, we will be able to investigate the incidence rate of PRGs in different environments as WALLABY will cover the majority of the southern sky. This will remove a source of cosmic variance that may cause our large estimated incidence rate.

Yet another possible reason for the higher incidence rate is that H I rings may be an evolutionary stage in PRGs. In Bekki (1997), simulations of PRG formation showed that

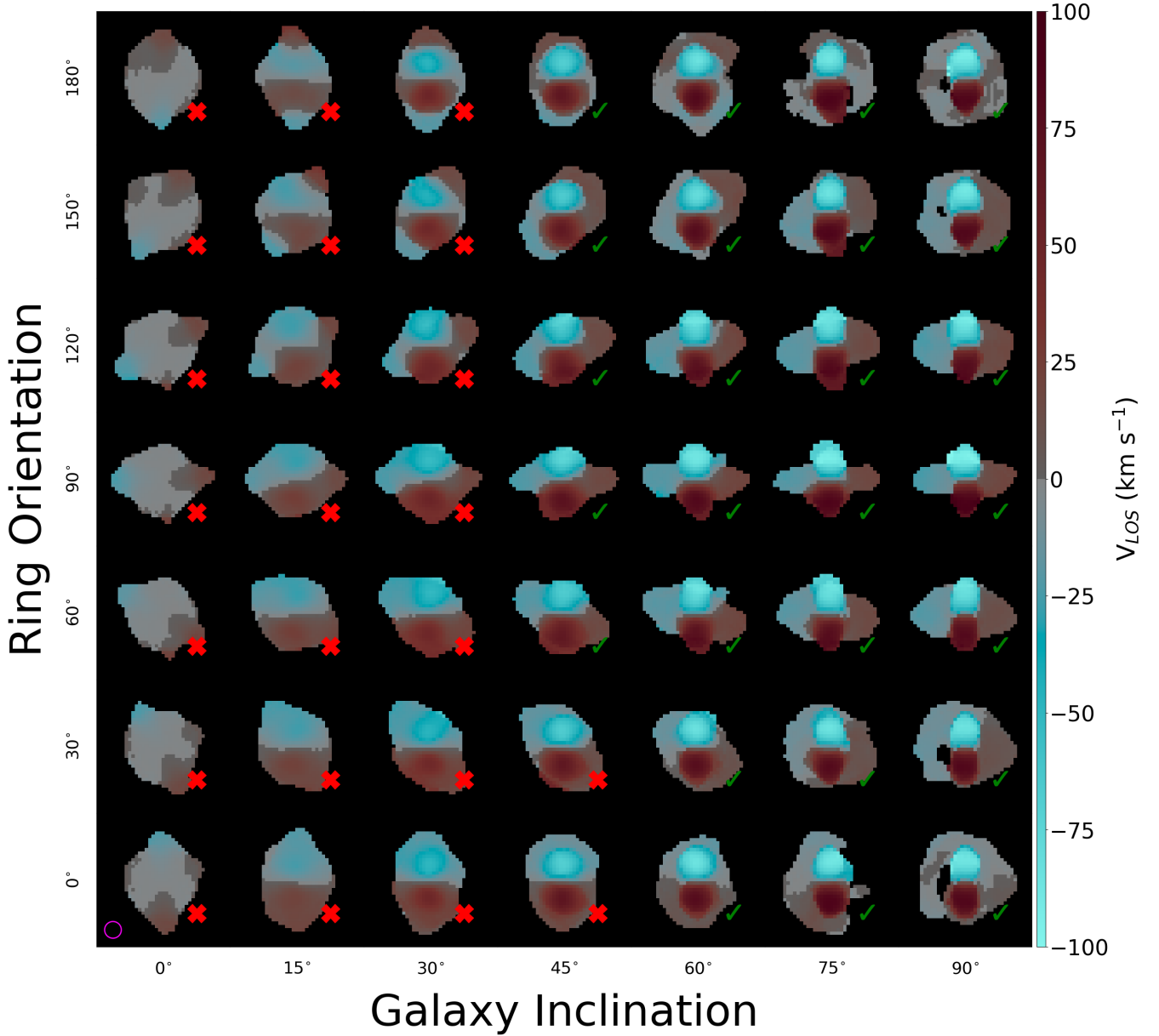


Figure 14. Same as Figure 11, but for the moment 1 maps of different projections of the best fitting H I PRG model of NGC 6156 at a 6 beam resolution.

star formation converted some of the gas in PRGs to stars. It is possible that our potential H I PRGs may eventually evolve into stellar PRGs (assuming that the morphology is correct). However, simulations also show that polar structures are not permanent (Khoperskov et al. 2021). If this evolution picture is correct, some PRGs would first form in H I then convert to optical structures, and finally fall back to the galaxy disk. In such a situation, it may be that the H I rings last longer than optical rings, leading to a higher incidence rate. To investigate this idea detailed observations of the optical counterparts to the anomalous gas will be necessary to determine the local star formation rates.

If PRGs are indeed more common than previously estimated, WALLABY will find an abundance of new PRGs. Predictions for the full WALLABY survey contained in Ko-

ribalski et al. (2020) indicate that $\geq 10^4$ galaxies will be resolved by ≥ 5 beams. If the detection rate found in PDR1 holds true, this implies that WALLABY will detect hundreds of PRGs. Moreover, WALLABY plans to observe a subset of galaxies at a higher angular resolution of $\sim 10''$. This increased resolution means that most of those "postage stamps" will be resolved enough to see polar rings or other large scale kinematic misalignments. However, it is important to recognize that our incidence rate estimate is based on only two galaxies, which is well within the realm of Poisson statistics. As WALLABY moves into the future, this possibility will rapidly be resolved. Accurately measuring the rate of PRGs and the more general rate of extreme kinematic misalignments in gas is an interesting probe of galaxy formation. Large scale cosmological simulations are producing

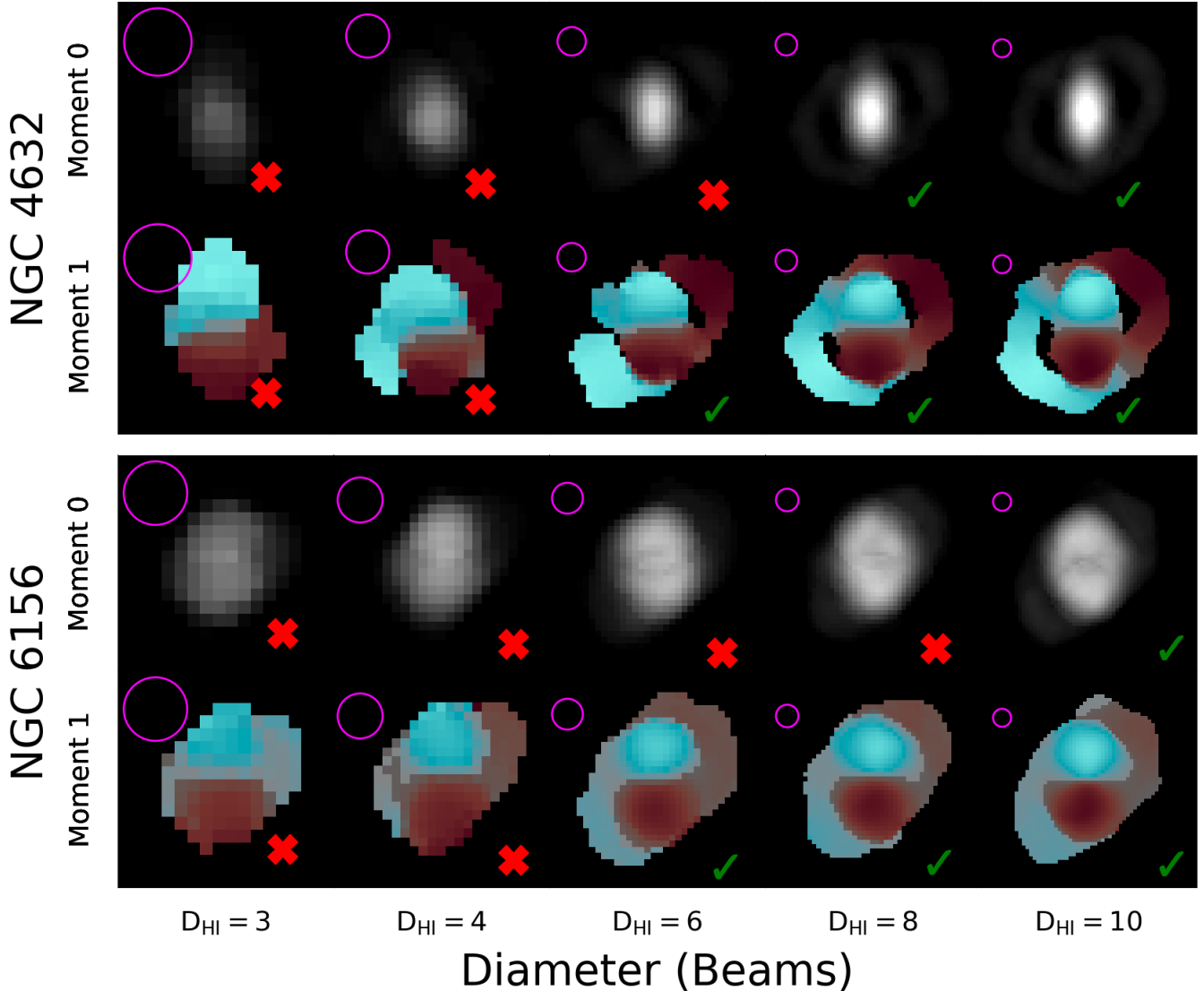


Figure 15. A demonstration of how angular resolution affects the detectability of H I PRGs from both moment 0 and moment 1 maps. This figure shows both galaxies at a single orientation ($i = 45^\circ$, $\beta = 30^\circ$) at the five resolutions that were examined. The circles at the top left corner of each frame represents the beam size for that figure. The green checkmarks and red x's indicate panels where we were able or unable to determine the galaxy is PRG based on the specific moment map respectively.

these types of objects (e.g. Macciò et al. 2006; Roškar et al. 2010), which will allow a comparison between the observed and simulated formation rates similar to the work of Elagali et al. (2018) on the formation of ring galaxies (where there is a stellar ring in the disk plane that are generally formed by drop through interactions).

Regardless of the precise PRG rate, the two potential H I PRGs found in WALLABY PDR1 are exciting and unique objects. Unlike most PRGs, they have been detected in H I rather than in stellar structures, they are gas rich, and we have been able to construct plausible kinematic models for the galaxies. As better observations and more sophisticated models are obtained for both galaxies, it will be possible to constrain the parameters of the ring progenitor (if they are indeed formed via mergers or flybys). Understanding

whether these are from interactions or gas accretion will provide constraints on galaxy formation and evolution.

ACKNOWLEDGEMENT

We would like to thank the anonymous referee for their helpful comments and suggestions. Thanks to G. Meurer for useful comments.

This scientific work uses data obtained from Inyarrimanha Ilgari Bundara / the Murchison Radio-astronomy Observatory. We acknowledge the Wajarri Yamaji People as the Traditional Owners and native title holders of the Observatory site. The Australian SKA Pathfinder is part of the Australia Telescope National Facility (<https://ror.org/05qajvd42>) which is managed by CSIRO.

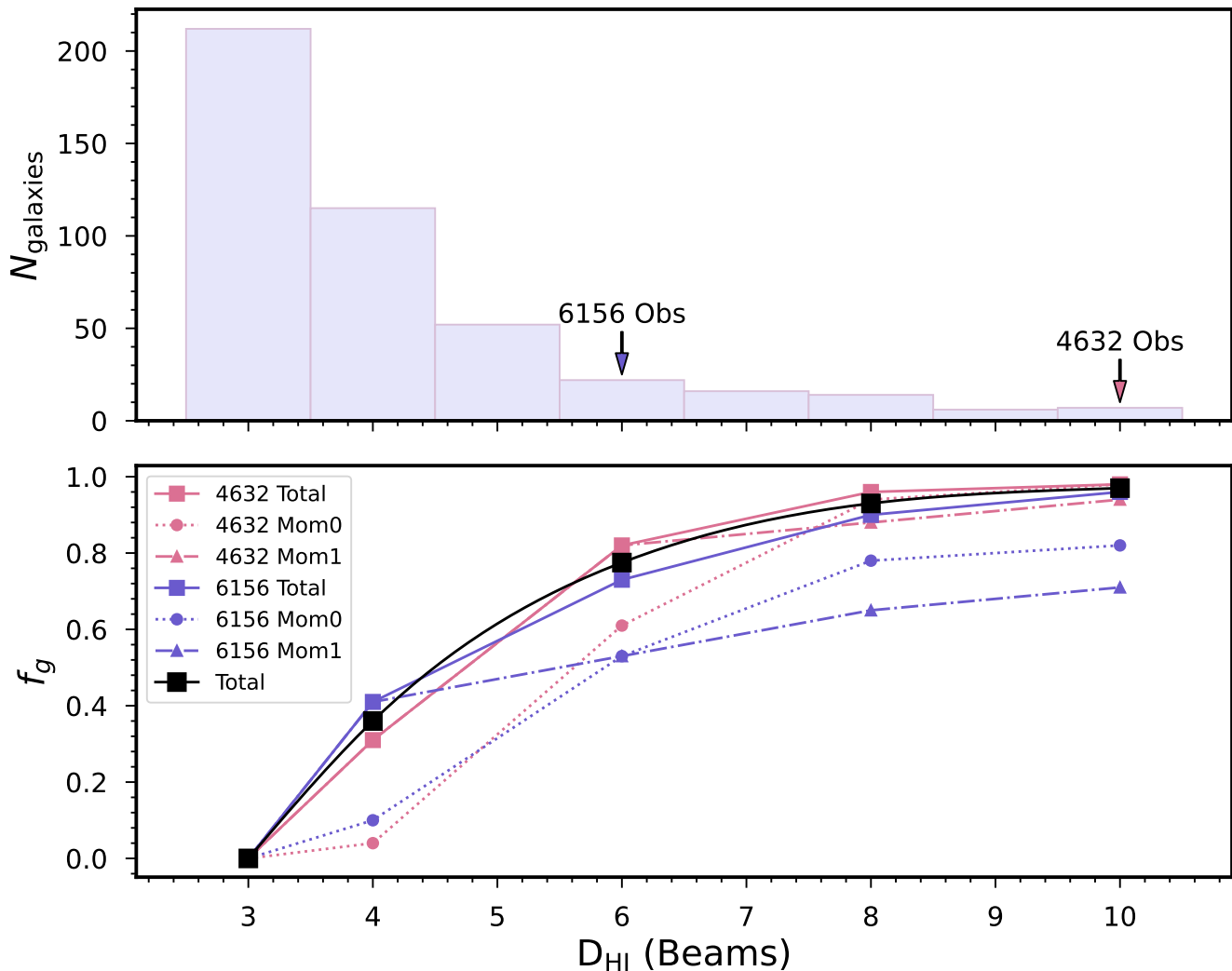


Figure 16. The number of observed PDR1 galaxies as a function of the number of beams across the major axis of that detection (top panel), and the estimated fraction of HI PRGs that would be detectable at that resolution (bottom panel). In the top panel, the arrows indicate the resolution of each the detected potential HI PRGs. In the bottom panel, the dotted, dashed and solid lines represent the detectability fraction from moment 0, moment 1 and the combination of moment 0 and moment 1 information respectively for the NGC 4632 model (magenta) and the NGC 6156 model (blue).

Operation of ASKAP is funded by the Australian Government with support from the National Collaborative Research Infrastructure Strategy. ASKAP uses the resources of the Pawsey Supercomputing Centre. Establishment of ASKAP, the Murchison Radio-astronomy Observatory and the Pawsey Supercomputing Centre are initiatives of the Australian Government, with support from the Government of Western Australia and the Science and Industry Endowment Fund.

WALLABY acknowledges technical support from the Australian SKA Regional Centre (AusSRC) and Astronomy Data And Computing Services (ADACS).

This research uses services or data provided by the Astro Data Lab at NSF's National Optical-Infrared Astronomy Research Laboratory. NOIRLab is operated by the Association of Universities for Research in Astronomy (AURA),

Inc. under a cooperative agreement with the National Science Foundation.

This publication makes use of data products from the Wide-field Infrared Survey Explorer, which is a joint project of the University of California, Los Angeles, and the Jet Propulsion Laboratory/California Institute of Technology, funded by the National Aeronautics and Space Administration.

This work made use of the Inter-University Institute for Data Intensive Astronomy (IDIA) visualization lab⁵. IDIA is a partnership of the University of Cape Town, the University of Pretoria and the University of the Western Cape. This work made use of the iDaVIE-v (immersive Data Visualisation Interactive Explorer for volumet-

⁵ <https://vislab.idia.ac.za>

ric rendering) software (DOI - 10.5281/zenodo.4614116 - <https://idavie.readthedocs.io/>)

Parts of this research were supported by the Australian Research Council Centre of Excellence for All Sky Astrophysics in 3 Dimensions (ASTRO 3D), through project number CE170100013.

T.H.J. acknowledges support from the National Research Foundation (South Africa). AB acknowledges support from the Centre National d'Etudes Spatiales (CNES), France. P.K. is supported by the BMBF project 05A20PC4 for D-MeerKAT. K.S. acknowledges support from the Natural Sciences and Engineering Research Council of Canada (NSERC).

DATA AVAILABILITY

The WALLABY data are available through the [WALLABY data access portal](#) at both the CSIRO ASKAP Science Data Archive (CASDA) and the Canadian Astronomy Data Center (CADC). The galaxy models and modelling scripts will be shared upon request to the corresponding author.

REFERENCES

- Aihara H., et al., 2018, *PASJ*, **70**, S8
- Ann H. B., Park J. C., 2006, *New Astron.*, **11**, 293
- Ann H. B., Seo M., Ha D. K., 2015, *ApJS*, **217**, 27
- Arnaboldi M., Oosterloo T., Combes F., Freeman K. C., Koribalski B., 1997, *AJ*, **113**, 585
- Bait O., Kurapati S., Duc P.-A., Cuillandre J.-C., Wadadekar Y., Kamphuis P., Barway S., 2020, *MNRAS*, **492**, 1
- Begeman K. G., 1989, *A&A*, **223**, 47
- Bekiaris G., Glazebrook K., Fluke C. J., Abraham R., 2016, *MNRAS*, **455**, 754
- Bekki K., 1997, *ApJ*, **490**, L37
- Bournaud F., Combes F., 2003, *A&A*, **401**, 817
- Brook C. B., Governato F., Quinn T., Wadsley J., Brooks A. M., Willman B., Stilp A., Jonsson P., 2008, *ApJ*, **689**, 678
- Bundy K., et al., 2015, *ApJ*, **798**, 7
- Buson L. M., Bettoni D., Galletta G., 2011, *Ap&SS*, **335**, 231
- Cao X., et al., 2022, *Nature Astronomy*, **6**, 1464
- Cappellari M., et al., 2011, *MNRAS*, **413**, 813
- Catinella B., et al., 2018, *MNRAS*, **476**, 875
- Cluver M. E., Jarrett T. H., Dale D. A., Smith J. D. T., August T., Brown M. J. I., 2017, *ApJ*, **850**, 68
- Combes F., Arnaboldi M., 1996, *A&A*, **305**, 763
- Comrie A., Sivitilli A., Vitello F., Jarrett T., Marchetti L., 2021, iDaVIE-v: Immersive Data Visualisation Interactive Explorer for Volumetric Rendering, Zenodo, [doi:10.5281/zenodo.4614116](https://doi.org/10.5281/zenodo.4614116)
- Davis T. A., et al., 2013, *MNRAS*, **429**, 534
- De Rijcke S., Buyle P., Koleva M., 2013, *ApJ*, **770**, L26
- Deg N., et al., 2022, *Publ. Astron. Soc. Australia*, **39**, e059
- Demers S., Battinelli P., Kunkel W. E., 2006, *ApJ*, **636**, L85
- Di Teodoro E. M., Fraternali F., 2015, *MNRAS*, **451**, 3021
- Džudžar R., Kilborn V., Sweet S. M., Meurer G., Jarrett T. H., Kleiner D., 2021, *MNRAS*, **500**, 3689
- Elagali A., Lagos C. D. P., Wong O. I., Staveley-Smith L., Trayford J. W., Schaller M., Yuan T., Abadi M. G., 2018, *MNRAS*, **481**, 2951
- García-Ruiz I., Sancisi R., Kuijken K., 2002, *A&A*, **394**, 769
- Ho L. C., Li Z.-Y., Barth A. J., Seigar M. S., Peng C. Y., 2011, *ApJS*, **197**, 21
- Hotan A. W., et al., 2021, *Publ. Astron. Soc. Australia*, **38**, e009
- Jarrett T. H., et al., 2013, *AJ*, **145**, 6
- Jarrett T. H., Cluver M. E., Brown M. J. I., Dale D. A., Tsai C. W., Masci F., 2019, *ApJS*, **245**, 25
- Jarrett T. H., et al., 2021, *Astronomy and Computing*, **37**, 100502
- Jarrett T. H., Cluver M. E., Taylor E. N., Bellstedt S., Robotham A. S. G., Yao H. F. M., 2023, *ApJ*, **946**, 95
- Johnston S., et al., 2008, *Experimental Astronomy*, **22**, 151
- Józsa G. I. G., Kenn F., Klein U., Oosterloo T. A., 2007, *A&A*, **468**, 731
- Józsa G. I. G., Oosterloo T. A., Morganti R., Klein U., Erben T., 2009, *A&A*, **494**, 489
- Kamphuis P., Józsa G. I. G., Oh S.-H., Spekkens K., Urbancic N., Serra P., Koribalski B. S., Dettmar R. J., 2015, *MNRAS*, **452**, 3139
- Khoperskov S. A., Moiseev A. V., Khoperskov A. V., Saburova A. S., 2014, *MNRAS*, **441**, 2650
- Khoperskov S., et al., 2021, *MNRAS*, **500**, 3870
- Koribalski B. S., et al., 2020, *Ap&SS*, **365**, 118
- Lee B., et al., 2022, *ApJS*, **262**, 31
- Lewis C., 2019, PhD thesis, Queen's University at Kingston, Canada
- Lintott C. J., et al., 2008, *MNRAS*, **389**, 1179
- Macciò A. V., Moore B., Stadel J., 2006, *ApJ*, **636**, L25
- Moiseev A. V., Smirnova K. I., Smirnova A. A., Reshetnikov V. P., 2011, *MNRAS*, **418**, 244
- Morales G., Martínez-Delgado D., Grebel E. K., Cooper A. P., Javanmardi B., Miskolczi A., 2018, *A&A*, **614**, A143
- Nishimura M., Matsubayashi K., Murayama T., Taniguchi Y., 2022, arXiv e-prints, [p. arXiv:2208.12388](https://arxiv.org/abs/2208.12388)
- Oh S.-H., Staveley-Smith L., Spekkens K., Kamphuis P., Koribalski B. S., 2018, *MNRAS*, **473**, 3256
- Punzo D., van der Hulst J. M., Roerdink J. B. T. M., Fillion-Robin J. C., Yu L., 2017, *Astronomy and Computing*, **19**, 45
- Querejeta M., et al., 2015, *ApJS*, **219**, 5
- Reshetnikov V. P., Mosenkov A. V., 2019, *MNRAS*, **483**, 1470
- Reshetnikov V., Sotnikova N., 1997, *A&A*, **325**, 933
- Reshetnikov V. P., Faúndez-Abans M., de Oliveira-Abans M., 2011, *Astronomy Letters*, **37**, 171
- Ristea A., et al., 2022, *MNRAS*, **517**, 2677
- Rogstad D. H., Lockhart I. A., Wright M. C. H., 1974, *ApJ*, **193**, 309
- Roškar R., Debattista V. P., Brooks A. M., Quinn T. R., Brook C. B., Governato F., Dalcanton J. J., Wadsley J., 2010, *MNRAS*, **408**, 783
- Sackett P. D., Sparke L. S., 1990, *ApJ*, **361**, 408
- Sandage A., 1961, The Hubble Atlas of Galaxies
- Sandage A., Bedke J., 1994, The Carnegie atlas of galaxies. Vol. 638
- Sanders D. B., Mazzarella J. M., Kim D. C., Surace J. A., Soifer B. T., 2003, *AJ*, **126**, 1607
- Schechter P. L., Gunn J. E., 1978, *AJ*, **83**, 1360
- Schimminovich D., van Gorkom J. H., van der Hulst J. M., 2013, *AJ*, **145**, 34
- Serra P., et al., 2012, *MNRAS*, **422**, 1835
- Serra P., et al., 2014, *MNRAS*, **444**, 3388
- Serra P., et al., 2015, *MNRAS*, **448**, 1922
- Sheth K., et al., 2010, *PASP*, **122**, 1397
- Smirnov D. V., Reshetnikov V. P., 2022, *MNRAS*, **516**, 3692
- Stanonik K., Platen E., Aragón-Calvo M. A., van Gorkom J. H., van de Weygaert R., van der Hulst J. M., Peebles P. J. E., 2009, *ApJ*, **696**, L6
- Tully R. B., Courtois H. M., Sorce J. G., 2016, *AJ*, **152**, 50
- Warner P. J., Wright M. C. H., Baldwin J. E., 1973, *MNRAS*, **163**, 163
- Werner M. W., et al., 2004, *ApJS*, **154**, 1
- Westmeier T., et al., 2021, *MNRAS*, **506**, 3962
- Westmeier T., et al., 2022, *Publ. Astron. Soc. Australia*, **39**, e058

- Whitmore B. C., Lucas R. A., McElroy D. B., Steiman-Cameron T. Y., Sackett P. D., Olling R. P., 1990, *AJ*, **100**, 1489
- Zhang S., Mackey D., Da Costa G. S., 2021, *MNRAS*, **508**, 2098
- de Vaucouleurs G., de Vaucouleurs A., Corwin Herold G. J., Buta R. J., Paturel G., Fouque P., 1991, Third Reference Catalogue of Bright Galaxies
- van Gorkom J. H., Schechter P. L., Kristian J., 1987, *ApJ*, **314**, 457
- van der Hulst J. M., Terlouw J. P., Begeman K. G., Zwitser W., Roelfsema P. R., 1992, in Worrall D. M., Biemesderfer C., Barnes J., eds, *Astronomical Society of the Pacific Conference Series Vol. 25, Astronomical Data Analysis Software and Systems I*. p. 131

APPENDIX A: WARPED AND RING MODELLING

While this paper has focused on whether NGC 4632 and NGC 6156 are consistent with perfectly polar models, it is possible that they are extreme warps or inclined rings/disks. In this appendix we explore this wider range of possible models.

A1 ‘Warped’ Models

As a part of the WALLABY PDR1 kinematic modelling efforts (Deg et al. 2022), both NGC 4632 and NGC 6156 were attempted to be modelled as ‘flat disks’ (i.e. with constant geometries) using their proto-pipeline that combines both 3DBAROLO and FAT. These models were deemed to be failures due to the kinematic misalignment between the inner disk and anomalous gas apparent in the data.

Given the failure of the flat disk models, it is reasonable to use 3DBAROLO to fit a ‘warped’ model for each galaxy. In this approach, the inclination and position angle of the model are left as free parameters. It is worth noting that these are sky plane coordinates and must be transformed to galaxy plane coordinates in order to determine the orientation of the anomalous gas with respect to the inner galaxy. 3DBAROLO has a number of potential switches and modes that can be optimized for a particular modelling attempt. In this case we used the ‘two-stage’ mode, which fits the galaxy twice. First it does a TR fitting of all the parameters of all rings separately. Then it fits the resulting inclination and position angle profiles by a bezier function. Those fitted geometric parameters are fixed in the second TR fitting of the data. As such the final inclination and position angle parameters are not given with any uncertainties. Nonetheless, the average uncertainties of the first fit can be used as approximate uncertainties on the inclination and position angle.

Figure A1 shows the results of this two-stage warped 3DBAROLO fit to the data. There are a number of key features to discuss in this fit. Firstly, in this model, the inner orientation of the galaxy has $(i_g, PA_g) \approx (60^\circ, 55^\circ)$, while the anomalous gas has an orientation of $(i_r, PA_r) \approx (52^\circ, 20^\circ)$. This orientation implies that the anomalous gas is inclined at 30° relative to the galaxy plane of NGC 4632. Such an orientation would make NGC 4632 a warped galaxy and not a PRG. However, this model does not reproduce the separation of the anomalous gas from the inner galaxy that is seen in panel A of the figure. Additionally, the model velocity map shows an ‘S’ shaped curve that roughly

traces out the V_{sys} that is more pronounced than the observations. Additionally, the systemic velocity appears to be slightly different from the galaxy’s systemic velocity, as seen by the offset of the grey regions in the two moment 1 panels.

A similar exercise can be done for NGC 6156. Figure A2 shows the results of this analysis. In this case 3DBAROLO has failed to model the anomalous gas. The modelled systemic velocity appears to be slightly offset from the data as well.

A2 Inclined Ring Models

The failure of the warped NGC 6156 model, as well as the fact that the warped NGC 4632 does not fully reproduce some key features of the anomalous gas, are chiefly due to the low S/N and resolution of the data. Complex models that consider the full parameter space of anomalous gas orientations are difficult to constrain with such data. However, slightly less complex models can be used to answer more restricted questions. One approach is to use 3DBAROLO to model the inner disk and anomalous gas separately as individual flat disk models. This approach assumes that the anomalous gas can be described as a discrete ring or disk structure and does not consider warped models.

While such double flat disk models are simpler than the full 3DBAROLO models explored earlier, there are a number of important details to discuss. Firstly, there is the separation of the inner galaxy from the anomalous gas. For this work, we use the masks generated by the iDAVIE separation discussed in Sec. 2. These are seen in middle rows of Figs. 2 and 3. For both cases, a comparison of the middle (galaxy body) and bottom (anomalous gas) rows shows that the masking has isolated the main bodies of the galaxies quite well. In particular, for NGC 6156, the apparently Gaussian profile has been transformed into a more standard, albeit noisy, flat/double-peaked profile.

Upon separation of the galaxy into the inner and outer components, a first ‘flat-disk’ fit to the inner disk is required. This fit starts with an estimate of the initial parameters, but, when the data has a low S/N and resolution like both our galaxies, the initial estimates on the parameters have a strong influence on the final model. In particular the initial estimate for the inclination provides strongly affects the results. For this particular analysis, we have adopted an optical inclination of $\sim 62.5^\circ$ based on the HSC image. For this inner disk fit, all geometric parameters as well as the rotation curve and surface density profile are fit by 3DBAROLO using the *two-stage* fitting option. This particular fitting option fits the galaxy twice, and in the second fit, the geometric parameters are fixed based on the results of the first fitting step. In order to keep the separate fits for the inner and outer disk consistent, the outer disk center point and systemic velocity are fixed to the results of the inner disk ‘flat-disk’ model.

Figure A3 shows the results for a combined model from individual flat disk fits to the inner galaxy and anomalous gas components using 3DBAROLO. In this case, the fit to the anomalous gas is clearly distinct from the inner disk, which the warped was unsuccessful at replicating. In this model, the outer structure is inclined at $\sim 24^\circ$ with respect to the inner disk. However, the moment 0 map of the model shows that the shape and extent of the outer model

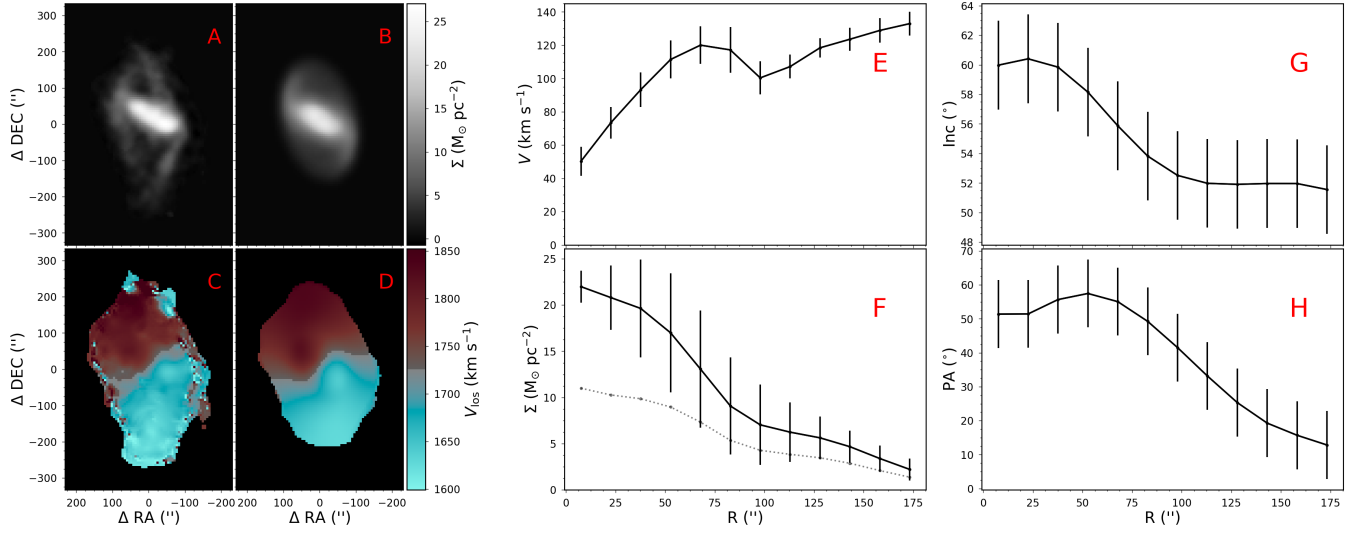


Figure A1. The best fitting 3DBAROLO warped model for NGC 4632. Panels and lines are as in 9 with the exception of the dashed black line in Panel F. This line shows the face-on surface density profile provided by the 3DBAROLO warped galaxy fit.

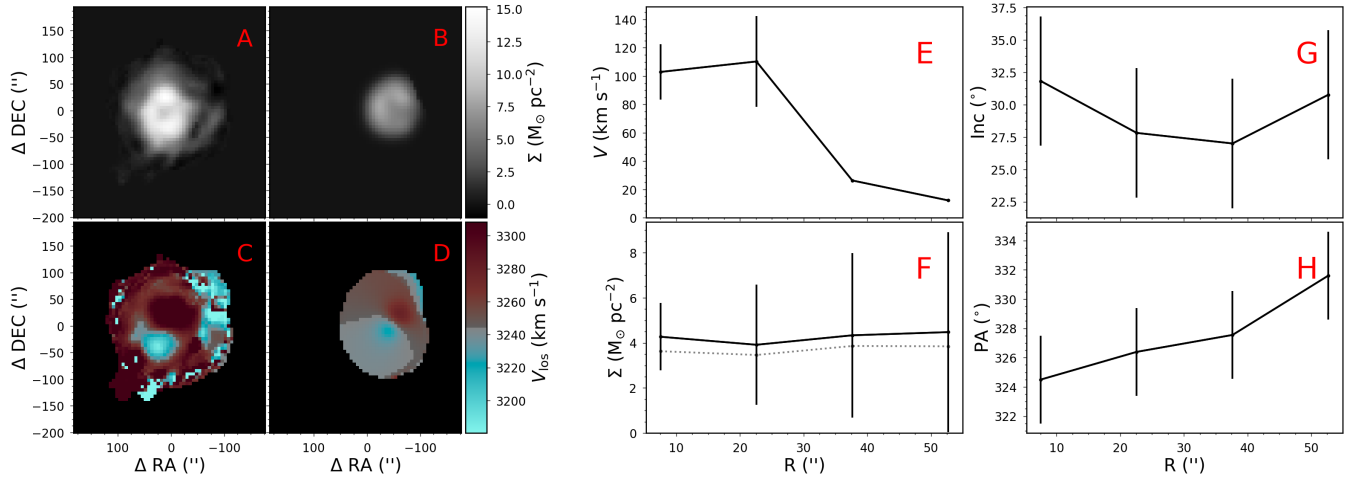


Figure A2. The best fitting 3DBAROLO warped model for NGC 6156. Panels and lines are as in A1.

does not match the observed structure of the anomalous gas. And, while the moment 1 map no longer shows the ‘S’ shape for the systemic velocity, a separation between the different components velocity structures can be seen that is not as clear in the actual observations.

Given the results of these combined fit for NGC 4632 as well as the poorer S/N and resolution of the NGC 6156 data, we have chosen not to generate a combined model for NGC 6156. One of the potential reasons for these poor results is a particular quirk of 3DBAROLO. When 3DBAROLO is passed a mask, whether it be the WALLABY SOF1A masks used for the warped models or the inner and outer masks for the combined models, 3DBAROLO still runs its source finding algorithm. Rather than examining the full cube, it restricts the source finding to the masked region. This works well for the initial problems that 3DBAROLO was designed to address, but it causes issues here. It is likely that the 3DBAROLO source finding is not extracting the full

content of the anomalous gas (although it is likely working quite well on the inner disk), leading to poor fits for both the warped and combined models.

Comparing the results of these more general modelling approaches for both NGC 4632 and NGC 6156 to the purely polar models of Sec. 4, it is clear that there all three types of models have the ability to reproduce the data. Given the issues in each fit, we are unable to definitively determine the morphology of the anomalous gas. Thus, even though our observations are *consistent* with PRG models, we cannot rule out warped or inclined ring models. Without improved observations, we must continue to classify these as *potential* PRGs.

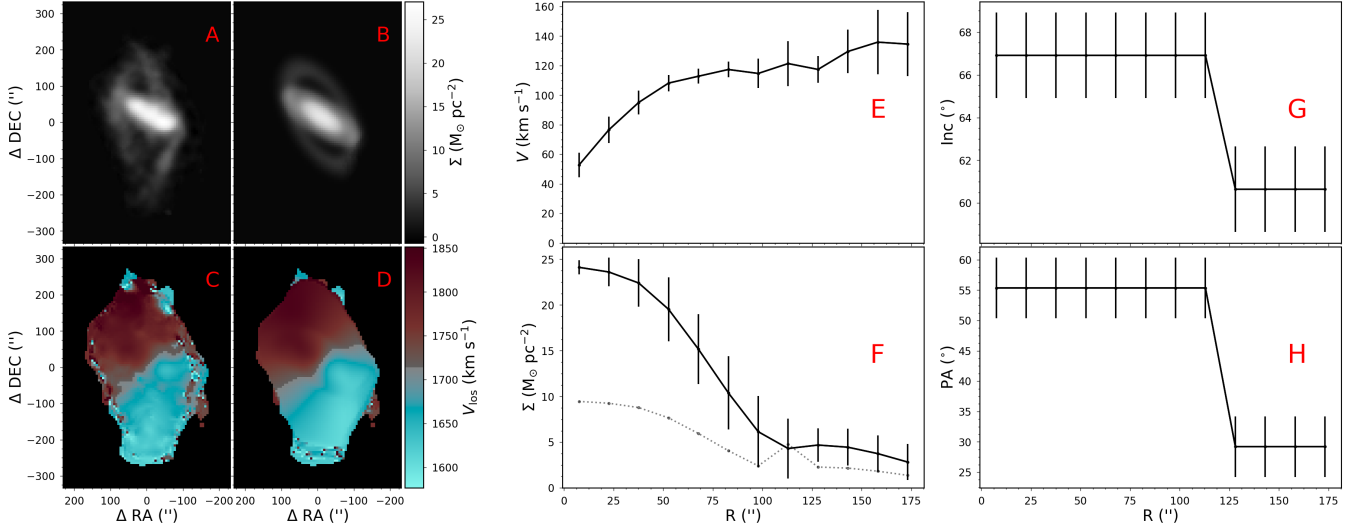


Figure A3. A combined model from individual flat disk 3DBAROLO fits to the inner disk and anomalous components of NGC 4632. Panels and lines are as in A1.

APPENDIX B: PERFECTLY POLAR RING GEOMETRY

This appendix contains a derivation of the perfectly polar ring relations in Equations 1 and Eq. 2 that underpin the kinematic models in Sec. 4.2. They arise from the transformation of points between three coordinate systems; the sky plane, the galaxy plane, and the ring plane. These transformations are accomplished using rotations where the rotation angles are related to physical quantities.

In the most general sense, the transformation of points in galaxy plane to the sky plane is

$$\mathbf{x}_s = R_z(\theta_g)R_x(i_g)\mathbf{x}_g, \quad (\text{B1})$$

where \mathbf{x}_s are the sky-plane coordinates, \mathbf{x}_g are the galaxy plane coordinates, $R_x(i_g)$ is a rotation about the x_g axis by the inclination i_g , $\theta_g = PA_g + 90^\circ$, and $R_z(\theta_g)$ is a rotation about the z_g axis by θ_g . A similar transformation will convert points in the ring plane to points in the sky plane

$$\mathbf{x}_s = R_z(\theta_r)R_x(i_r)\mathbf{x}_r, \quad (\text{B2})$$

where the model polar ring is assumed to have the same geometric center as the galaxy body. Filling in the matrices, the transformation becomes

$$\mathbf{x}_s = \begin{pmatrix} c_{\theta_r} & -s_{\theta_r}c_{i_r} & s_{\theta_r}s_{i_r} \\ s_{\theta_r} & c_{\theta_r}c_{i_r} & -c_{\theta_r}s_{i_r} \\ 0 & s_{i_r} & c_{i_r} \end{pmatrix} \mathbf{x}_r, \quad (\text{B3})$$

where c and s are the cos and sin functions respectively, and the subscript indicates the variable (i.e. $c_{\theta_r} = \cos(\theta_r)$).

Alternatively, it is possible to first transform points in the ring plane to the galaxy plane and then to the sky plane. A point in a polar ring can be transformed to galaxy plane coordinates via

$$\mathbf{x}_g = R_z(\beta)R_y(\phi)R_x(90^\circ)\mathbf{x}_r. \quad (\text{B4})$$

In this equation, we have introduced an extra rotation of ϕ about the y axis. This rotation is required for the further rotation to the sky plane coordinates. However, it is confusing from the point of view of a rotating circular ring of uniform

density, since that coordinate is morphologically degenerate. If the polar ring were to have an overdensity at some location, then ϕ would control where that overdensity appears on the sky.

Combining Equations B1 and B4 gives

$$\mathbf{x}_s = R_z(\theta_g)R_x(i_g)R_z(\beta)R_y(\phi)R_x(90^\circ)\mathbf{x}_r. \quad (\text{B5})$$

This can be simplified slightly by setting $\theta_g = 0$ to give

$$\mathbf{x}_s = R_x(i_g)R_z(\beta)R_y(\phi)R_x(90^\circ)\mathbf{x}_r. \quad (\text{B6})$$

This simplification does not lose any generality as the galaxy's position angle can simply be added to the ring's position angle once θ_r is calculated for $\theta_g = 0^\circ$. Filling in the rotation matrices gives

$$\mathbf{x}_s = \begin{pmatrix} c_\beta c_\phi & c_\beta s_\phi & s_\beta \\ c_{i_g} s_\beta c_\phi + s_{i_g} s_\phi & c_{i_g} s_\beta s_\phi - s_{i_g} c_\phi & -c_{i_g} c_\beta \\ s_{i_g} s_\beta c_\phi - c_{i_g} s_\phi & s_{i_g} s_\beta s_\phi + c_{i_g} c_\phi & -s_{i_g} c_\beta \end{pmatrix} \mathbf{x}_r. \quad (\text{B7})$$

Equating Eq. B3 to Eq. B7 gives a set of relations that can be used to solve for θ_r , i_r , and ϕ . This implies that ϕ is not a free rotation. It, like θ_r and i_r is uniquely determined by the (i_g, θ_g, β) angles. Using the [3,3] elements of the matrices (third row, third column), we get

$$c_{i_r} = -s_{i_g} c_\beta. \quad (\text{B8})$$

Similarly, dividing the [1,3] elements by the [2,3] elements gives

$$t_{\theta_r} = \frac{s_\beta}{c_\beta c_{i_g}}. \quad (\text{B9})$$

In this equation, we have not simplified the β terms in order to allow θ_r to vary across $0^\circ - 360^\circ$.

A key takeaway for this derivation is that a polar ring only has a specific range of allowed inclinations and position angles for a given galaxy body. For instance, for a face-on galaxy, the ring must be edge-on but can be at any position angle (determined by β). Conversely, when a galaxy is edge-on, the polar ring must have a position angle that lies at

90° to the galaxy's position angle, but it can be face-on or edge-on depending on the β angle.

This paper has been typeset from a $\text{\TeX}/\text{\LaTeX}$ file prepared by the author.